UNIVERSITY OF CALIFORNIA SAN DIEGO

Enabling an Anode-Free Sodium All-Solid-State Battery

A Dissertation submitted in partial satisfaction of the requirements
for the degree Doctor of Philosophy

in

Materials Science and Engineering

by

Grayson Deysher

Committee in charge:

Professor Shirley Meng, Chair
Professor Zheng Chen, Co-Chair
Professor Andrew Kummel
Professor Ping Liu

2024

The Dissertation of Grayson Deysher is approved, and it is acceptable in quality and form for publication on microfilm and electronically.

University of California San Diego

2024

DEDICATION

I dedicate this to my teachers Mrs. Bevis, Mr. Chappe, and Prof. Gogotsi.

TABLE OF CONTENTS

LIST OF FIGURES

LIST OF TABLES

LIST OF ABBREVIATIONS

SSE	Solid-State Electrolyte
XRD	X-ray Diffraction
EIS	Electrochemical Impedance Spectroscopy
SEM	Scanning Electron Microscopy
FIB	Focused-ion Beam
XPS	X-ray Photoelectron Spectroscopy
TEM	Transmission Electron Microscopy
DC	Direct Current
NPS	Na_3PS_4
NYZC	$Na_{2.25}Y_{0.25}Zr_{0.75}Cl_6$
NBH	$Na_4(B_{10}H_{10})(B_{12}H_{12})$

ACKNOWLEDGEMENTS

I would like to acknowledge Professor Shirley Meng for her support as my research advisor and the chair of my committee. Her guidance has proved to be invaluable.

Chapter 1, in part, is a reprint of the material as it appears in Evaluating Electrolyte–Anode Interface Stability in Sodium All-Solid-State Batteries. Deysher, Grayson; Chen, Yu-Ting; Sayahpour, Baharak; Lin, Sharon Wan-Hsuan; Ham, So-Yeon; Ridley, Phillip; Cronk, Ashley; Tan, Darren H. S.; Doux, Jean-Marie; Oh, Jin An Sam; Jang, Jihyun; Nguyen, Long Hoang Bao; Meng, Ying Shirley, ACS Applied Materials and Interfaces, 2022. The dissertation author was the primary author of this paper. Funding to support this work was provided by the National Science Foundation through the Partnerships for Innovation (PFI) grant no. 2044465. Additional support was provided by the National Science Foundation through the Future Manufacturing (FM) grant no. 2134764. This work was performed in part at the San Diego Nanotechnology Infrastructure (SDNI) of UCSD, a member of the National Nanotechnology Coordinated Infrastructure, which is supported by the National Science Foundation (grant ECCS-2025752). The authors acknowledge the use of facilities and instrumentation at the UC Irvine Materials Research Institute (IMRI), which is supported in part by the National Science Foundation through the UC Irvine Materials Research Science and Engineering Center (DMR-2011967). Specifically, the XPS work was performed using instrumentation funded in part by the National Science Foundation Major Research Instrumentation Program under grant no. CHE-1338173.

Chapter 2, in part, is a reprint of the material as it appears in An Anode-Free Sodium All-Solid-State Battery. Deysher, Grayson; Oh, Jin An Sam; Chen, Yu-Ting; Sayahpour, Baharak;

Ham, So-Yeon; Cheng, Diyi; Ridley, Phillip; Cronk, Ashley; Lin, Sharon Wan-Hsuan; Qian, Kun; Nguyen, Long Hoang Bao; Jang, Jihyun; Meng, Ying Shirley, Nature Energy, 2024. The dissertation author was the primary author of this paper. Funding to support this work was provided by the National Science Foundation through the Partnerships for Innovation (PFI) grant no. 2044465 received by Y. S. M. This work was performed in part at the San Diego Nanotechnology Infrastructure (SDNI) of UCSD, a member of the National Nanotechnology Coordinated Infrastructure, which is supported by the National Science Foundation (grant ECCS-2025752). The authors acknowledge the use of facilities and instrumentation at the UC Irvine Materials Research Institute (IMRI), which is supported in part by the National Science Foundation through the UC Irvine Materials Research Science and Engineering Center (DMR-2011967). Specifically, the XPS work was performed using instrumentation funded in part by the National Science Foundation Major Research Instrumentation Program under grant no. CHE-1338173. Xe plasma FIB experiments were conducted at the University of Southern California in the Core Center of Excellence in Nano Imaging. We also acknowledge the use of the UCSD Crystallography Facility.

VITA

2019 Bachelor of Science in Materials Science and Engineering, Drexel University

2020 Master of Science in Materials Science and Engineering, University of California San Diego

2024 Doctor of Philosophy in Materials Science and Engineering, University of California San Diego

PUBLICATIONS

1. Deysher, G., et al, 2024. *Nature Energy,* (accepted/proofing stage) DOI: 10.26434/chemrxiv-2023-tkcd9
2. Deysher, G., et al, 2022. *ACS Applied Materials & Interfaces*, *14*(42), pp.47706-47715.
3. Deysher, G., et al, 2022. *Materials Today Physics*, *24*, p.100679.
4. Deysher, G., et al, 2019. *ACS nano*, *14*(1), pp.204-217.
5. Deysher, G., et al. 2018. *Materials Today*, *21*(10), pp.1064-1065.

FIELD OF STUDY

Major Field: Materials Science and Engineering
Studies in Solid-State Batteries
Professor Shirley Meng

ABSTRACT OF THE DISSERTATION

Enabling an Anode-Free Sodium All-Solid-State Battery

by

Grayson Deysher

Doctor of Philosophy in Materials Science and Engineering

University of California San Diego, 2024

Professor Shirley Meng, Chair
Professor Zheng Chen, Co-Chair

Anode-free batteries possess the optimal cell architecture due to their reduced weight, volume, and cost. However, their implementation has been limited by unstable anode morphological changes and anode-liquid electrolyte interface reactions. An electrochemically stable solid electrolyte can solve these issues by enabling the deposition of dense sodium metal. Furthermore, a novel type of aluminum current collector can achieve intimate solid-solid contact with the solid electrolyte which allows highly reversible sodium plating and stripping at both high

areal capacities and current densities, previously unobtainable with conventional aluminum foil. A sodium anode-free all-solid-state battery full-cell is demonstrated with stable cycling for several hundred cycles. This cell architecture serves as a future direction for other battery chemistries to enable low-cost, high-energy-density, and fast charging batteries.

INTRODUCTION

Recent years have shown an increasing demand for electric vehicles as well as energy storage devices for large-scale grid applications. Batteries are critical for enabling these technologies and although they have improved significantly since the introduction of the first commercial lithium-ion battery in 1990 [1], further enhancements are needed to enable higher energy density and lower cost energy storage systems. Commonly used lithium is geographically concentrated and has experienced a significant increase in price as the demand for batteries grows [2]. Sodium-based materials, on the other hand, are significantly less expensive and more widely available. While sodium batteries are often assumed to sacrifice energy density in favor of lower cost, in this work we show that lower-cost sodium batteries may still achieve a high energy density comparable to current lithium systems due to the natural advantages of several sodium materials compared to their lithium counterparts.

To compete with the high energy density possessed by lithium-ion batteries, a significant change in sodium battery architectures is needed. A recently popularized idea is the use of an anode-free cell design [3]. Unlike conventional batteries, anode-free batteries are those in which no anode active material is used. Rather than using carbon- or alloy-based anode materials to store ions during cell charging, anode-free batteries rely on the electrochemical deposition of alkali metal directly onto the surface of a current collector (Fig. 1a). This achieves the lowest possible reduction potential, thus enabling higher cell voltage, lowers the cell cost, and increases energy density due to the removal of the anode active material (Fig. 1b).

However, many challenges have prevented the use of an anode-free architecture for both lithium and sodium chemistries. The deposition of lithium/sodium metal in conventional organic liquid electrolyte batteries is known to produce a porous or mossy-like morphology [4,5].

Additionally, liquid electrolytes commonly react with the deposited metal forming a solid-electrolyte interphase (SEI) [6–9]. Continuous anode morphological changes during cycling inevitably result in the continuous formation of SEI which steadily consumes the active material inventory [10]. Although several strategies have been explored including modifications to the liquid electrolyte [3,11–13], current collector [14], cell stack pressure [15], and cycling protocol [16], they have yielded only moderate improvements with many demonstrating only tens of cycles and/or low initial Coulombic efficiencies (ICE). Instead, a better approach is to utilize solid-state electrolytes. Due to their solid nature, the solid electrolyte separator layer is limited to a planar two-dimensional contact area with the negative electrode current collector (Fig. 1a). This can facilitate less solid-electrolyte interfacial reactions compared to large surface area three-dimensional anodes in liquid electrolyte systems. Furthermore, the use of applied stack pressure can enable a dense metal anode, which is required for mitigating contact loss, void formation, and cell short circuiting [17].

A few works have demonstrated a solid-state concept in lithium anode-free thin film batteries [18,19]; however these cell formats have limited areal capacities due to the thin cathode layers. Several recent works have attempted to enable anode-free cycling in bulk lithium solid-state cells using oxide- [20] or sulfide-based [21] solid electrolytes, however these cells also have exhibited poor reversibility. Several strategies have been explored for solving this challenge such as modifying the current collector [21], adding a sacrificial lithium sources [22,23], or incorporating lithiophilic alloying compounds like silver [24,25]. However, these strategies either fail to enable sufficiently reversible cycling or add inactive material to the cell which reduces the advantage of utilizing an anode-free design. To the best of our knowledge, only one recent attempt at making a sodium anode-free solid-state battery has been reported, although no electrochemical cycling was

demonstrated [26]. Therefore, it is critical to first determine the critical factors governing the performance of anode-free solid-state batteries.

To enable an anode-free sodium solid-state battery, four conditions must be met (Fig. 1c). First, an electrochemically stable or highly passivating electrolyte is needed to avoid the consumption of active sodium inventory due to the formation of a SEI layer. Second, intimate and robust solid-solid interface contact between the solid electrolyte and the current collector is needed for repeated sodium plating/stripping. Any void between the materials will prevent electron transfer and Na^0 deposition cannot occur. Third, a dense solid-state electrolyte separator is needed. It is known that pores, cracks, and imperfections can promote the growth of metal filaments through the separator resulting in cell short-circuiting [27–31]. Fourth, the current collector needs to be highly dense. While porous current collectors have been shown to be effective in liquid electrolyte cells due to their higher surface area and lowered local current densities [32,33], these current collectors cannot be used in solid-state cells. Unlike liquid electrolytes, solid-state electrolytes cannot flow into the pores of the current collector, therefore sodium plated inside the pores will become trapped due to the lack of sodium conduction pathways during stripping. If these four conditions are met, then an anode-free sodium all-solid-state battery can be enabled.

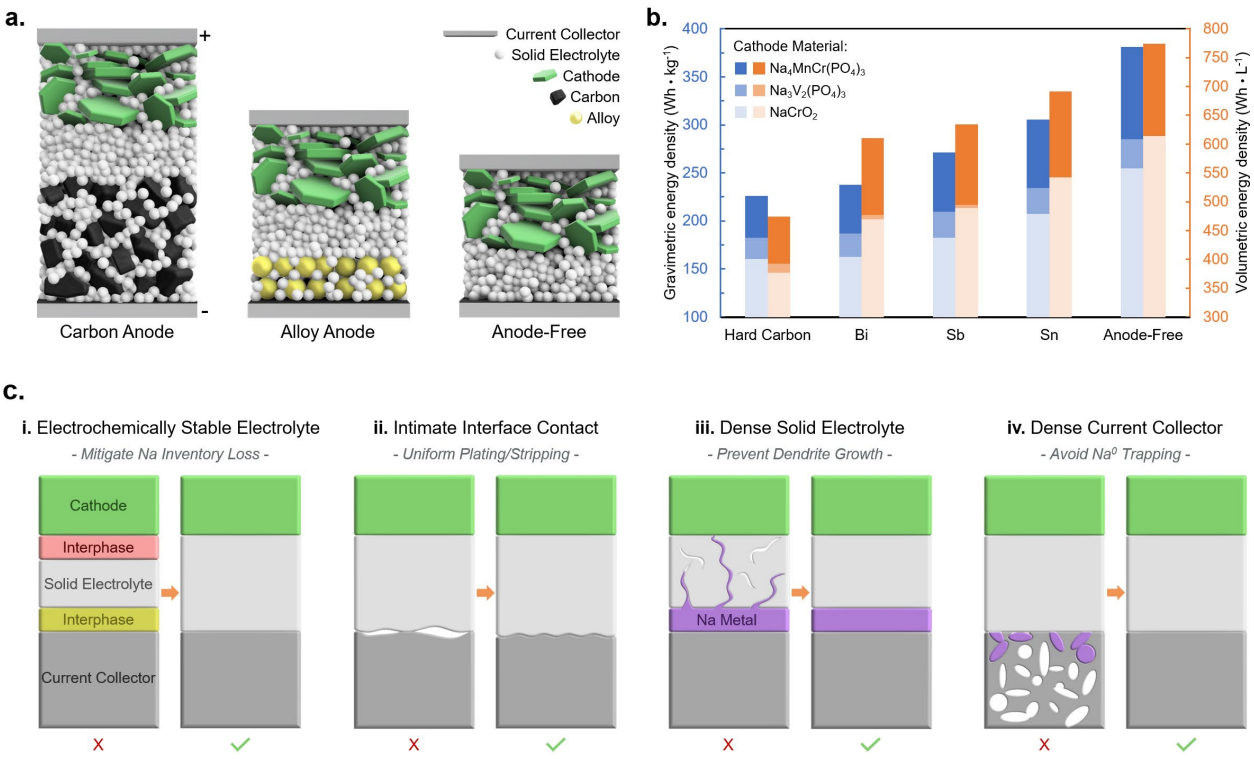

Figure 1. Anode-free schematics and energy density calculations. a) Cell schematic for carbon anodes, alloy anodes, and an anode-free configuration. b) Theoretical energy density comparison for various sodium anode materials. Values used for the calculations can be found in *table S1*. c) Schematic illustrating the requirements for enabling an anode-free all-solid-state battery.

Chapter 1 – Reduction Stability of Solid Electrolytes

Electrochemically Stable Electrolyte

An anode-free half-cell was assembled with the commonly used Na_3PS_4 (NPS) solid electrolyte paired with an aluminum foil current collector and Na_9Sn_4 counter electrode (Supplementary Figure 8). The ICE was 4%. This indicates that this solid electrolyte may not be stable against sodium metal as any instability can result in the low efficiency observed here. Therefore, it is critical to assess the electrochemical stability of this electrolyte in detail as well as other candidate materials to find one that is electrochemically stable and can enable stable sodium deposition and stripping.

Initial evaluation in full-cell configuration

Three Sn | SSE | $NaCrO_2$ composite full cells were assembled (SSE: NYZC, NPS, or NBH). The full cell system with a fixed amount of sodium was used to better understand the rate of Na inventory losses. Additionally, Sn was used as the anode instead of an anode-free configuration due to the more well known cyclability and reliability of Sn compared to anode-free cycling. In all cases, NYZC was used at the catholyte due to its oxidative stability (Supplementary Figure 1), along with an additional layer between the separator and the cathode to prevent direct contact between the cathode and the SSE of interest. The capacity ratio between the negative and positive electrodes (N/P ratio) was set at 1.2 for all three cells. The cell using NYZC as the separator showed rapid and irreversible failure, with a low initial Coulombic efficiency (ICE) of 12% (Figure 2a); its capacity faded rapidly to a negligible value after ten cycles. The cell using NPS showed a higher ICE of 62%, but a significant capacity fade was still observed over the first 10 cycles (Figure 2b). Among the three candidates, NBH showed the best ICE of 83% and capacity retention (Figure

2c). Interestingly, all three cells displayed a similar first charge capacity, indicating successful desodiation of the cathode. However, the cell discharge capacities exhibited stark differences. With the same Na inventory sent to the Sn anode in all three cells, the varying rates of Na inventory losses indicate that irreversible losses must therefore occur at the SSE–Sn interface. As the anode was pure Sn without any anolyte mixed in (i.e. not a composite anode), any interfacial degradation should occur at the contact plane between SSE and Sn electrode. To characterize the potential formation of an interphase, half cells using excess Na reservoir from a Na_9Sn_4 counter electrode was used. Excess Na allows higher capacity cycling which should amplify the effects of any interface reactions, enabling better detection and analysis.

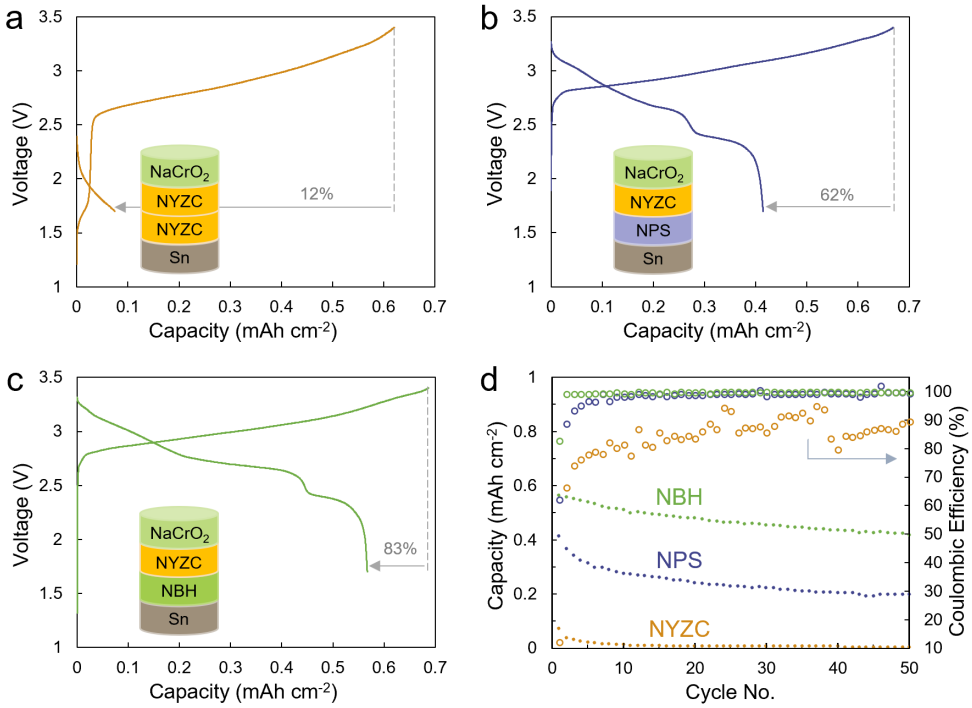

Figure 2. First cycle voltage curves of Sn | SSE | NYZC | Cathode composite cells using (a) NYZC, (b) NPS, and (c) NBH electrolytes. (d) Extended cycling data for the same three full cells. The cells were cycled at 0.064 mA·cm^{-2} (C/10).

SSE–Sn interface investigation

To examine the SSE–Sn interface, three half cells (Na_9Sn_4 | SSE | Sn) were constructed. After 24 h of contact, FIB milling was used to cut through the Sn and electrolyte layers to expose the 2D interface. In the pristine state, dense Sn and SSE layers were observed in all cells; no interface layer was observed for any of the electrolytes based on SEM imaging and Na elemental mapping (Figures 3a–c). This suggests that the pristine Sn electrode is chemically stable with the electrolytes. To further verify their chemically stable nature, Sn powder was mixed with each of the SSEs and heated for 10 h at 80 °C. After heating, XRD results (Supplementary Figure 2) showed that Sn and the pristine SSE remained intact. This suggests that even under harsh conditions, Sn is chemically stable with NYZC, NPS, and NBH. Besides chemical stability, electrochemical stability is the other important aspect to evaluate.

To probe the electrochemical stability of the SSEs with the (Na)Sn anode, the three half cells (Na_9Sn_4 | SSE | Sn) were cycled with the same Na capacity shuttling to the Sn electrode using a capacity cutoff protocol. The sodiated Na_xSn was then desodiated to a 2.0 V voltage cutoff (Figures 3d–f). Similar to the full cell cycling results (Figure 2), the same trend in Coulombic efficiency was observed for these half cells. NYZC was not able to cycle beyond the first Sn sodiation step and the overpotential of the cell quickly approached 4 V, indicating a significant increase in cell impedance. On the contrary, the NPS cell exhibited a higher efficiency (66%) while NBH exhibited the highest efficiency of 82%.

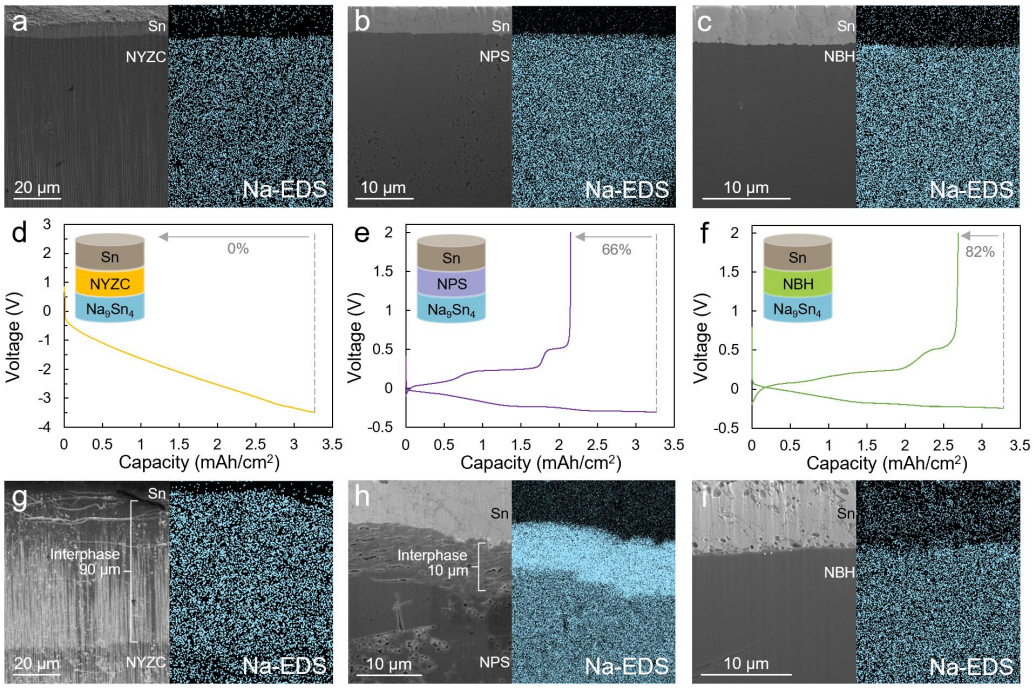

Figure 3. Cross-sections and Na-EDS mapping of the Sn|SSE interface of uncycled cells using (a) NYZC, (b) NPS, and (c) NBH electrolytes. Each cell was cycled once using 0.16 mA·cm^{-2} and the cycling data for (d) NYZC, (e) NPS, and (f) NBH are shown. Cross-sections and Na-EDS mapping of the Sn|SSE interface of the cells using (g) NYZC, (h) NPS, and (i) NBH electrolytes after cycling.

FIB milling was conducted after one cycle to probe the evolution of the SSE−Sn interface (Figures 3g–i). The interphase layers were characterized using EDS mapping to probe the Na concentration gradients to distinguish the SSE, Sn, and interphase layers. Any interlayer formed as a result of the reduction of the SSE would contain a higher concentration of Na compared to the pristine SSE. A 90 μm-thick interphase layer, highlighted by a high Na content, was observed in the cell with NYZC separator (Figure 3g). This finding correlates well with the observed cycling behavior, as such a thick interphase layer would be expected to cause a steep increase in the cell impedance and polarization (Figure 3d). For the NPS cell, a 10 μm-thick interphase layer was observed. Such a thinner interphase layer would result in less irreversible Na inventory consumption and a higher ICE (Figure 3e) compared to NYZC. Contrary to NYZC and NPS, no

interlayer was observed for the NBH cell; no noticeable change in the elemental mapping was seen at this interface (Supplementary Figure 3).

To further evaluate and quantify the effect of the formed interphase layers on cell impedance, EIS measurements were performed using the Na_9Sn_4 | SSE | Sn half-cell configuration, where the same areal capacity of Na (1.4 $mAh \cdot cm^{-2}$) was sent to the Sn electrode for all three cells (Figure 4). EIS measurements were conducted at five different intervals during the sodiation process to track any impedance growth (Figure 4a–c). Nyquist plots for NYZC, NPS, and NBH cells (Figures 4d–f) were fitted using the equivalent circuit shown in Figure 4d, and the interface resistance values are plotted in Figures 4g–i. For NYZC, the interfacial resistance increased by ~9000 Ω during the Sn sodiation, which agrees with the high polarization of the cell (Figure 4a). The interfacial degradation in NPS was less severe than NYZC as evidenced by a slight increase (~35 Ω) in the interfacial resistance (Figures 4b and 4h). On the other hand, the NBH cell exhibited negligible change in the interfacial resistance, implying the absence of any significant resistive layer at the Sn–NBH interface (Figure 4i).

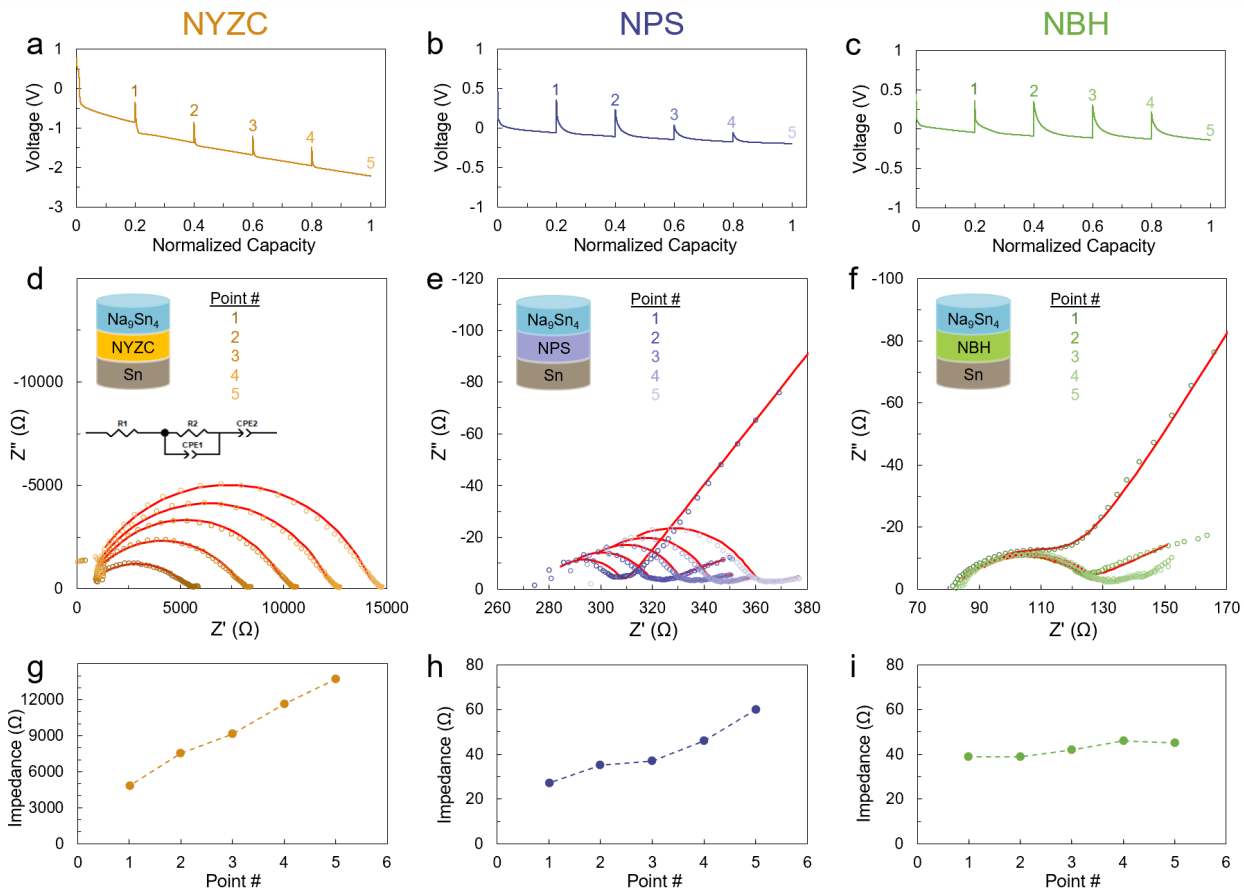

Figure 4. Voltage curves of Na_9Sn_4 | SSE | Sn half cells using (a) NYZC, (b) NPS, and (c) NBH electrolytes cycled at 0.16 $mA \cdot cm^{-2}$. Impedance growth during Sn sodiation for the Na_9Sn_4 | SSE | Sn half cells using (d) NYZC, (e) NPS, and (f) NBH electrolytes. Interfacial impedance growth during sodiation for (g) NYZC, (h) NPS, and (i) NBH based on the EIS fitting results.

SSE–Sn interface composition analysis

XPS was employed to identify the chemical composition of degradation products formed at the SSE−Sn interface (Figure 5). Three sets of samples were produced for each SSE: (i) pristine electrolytes as references, (ii) electrochemically sodiated samples recovered from the electrochemical cycling of Na_9Sn_4 | SSE | Sn half cells, and (iii) chemically sodiated samples obtained by directly mixing SSEs with Na metal. In the fabrication of electrochemically sodiated samples, extra SSE was intentionally added to the Sn electrode in the Na_9Sn_4 | SSE | Sn half cells to increase the contact area and amplify XPS signals corresponding to the degradation products.

All the chemically sodiated samples were subjected to XRD measurements for identification purposes.

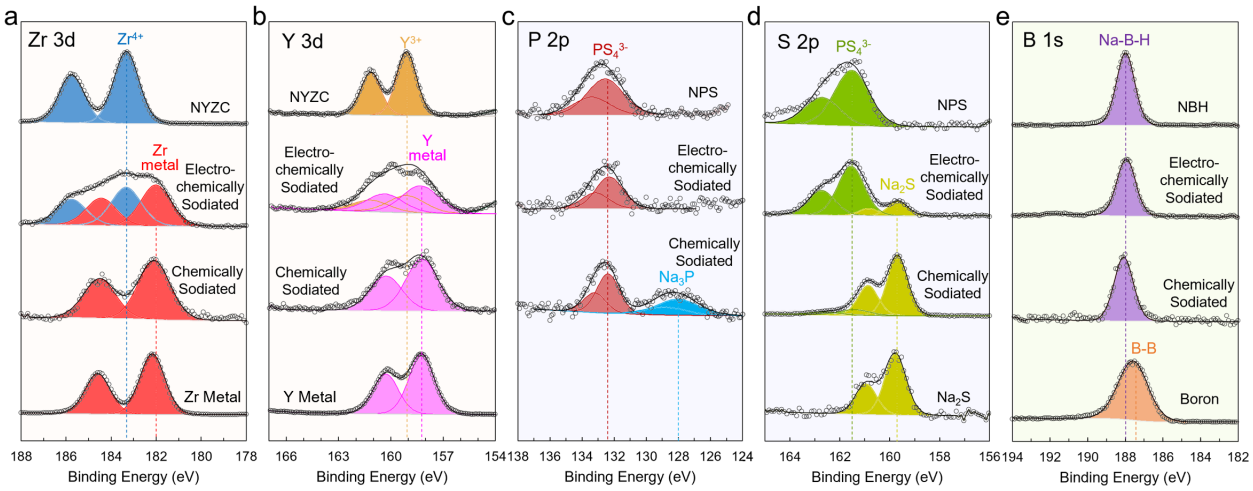

Figure 5. (a) Y 3d, (b) Zr 3d, (c) P 2p, (d) S 2p, and (e) B 1s XPS spectra for NYZC, NPS, NBH, and the electrochemically and chemically sodiated SSEs. Zr metal, Y metal, Na_2S and B are also added as references.

Zr and Y metal was detected in the electrochemically-sodiated NYZC as evidenced by the emergence of a new set of peaks at lower binding energies (Figures 5a–b). Peaks corresponding to pristine NYZC are still present in the electrochemically sodiated sample as part of the NYZC in the composite might not be in direct contact with Sn particles. When chemically sodiated, the XPS signatures of pristine NYZC completely disappeared and only Zr and Y metal peaks were observed. The XRD pattern of chemically sodiated NYZC only shows the diffraction peaks of NaCl, supporting a complete consumption of NYZC when it was in contact with Na metal (Figure 6a). The lack of any Bragg peaks associated with Y and Zr metals can be explained by the amorphization or the formation of nanocrystals that has been known to occur during the electrochemical cycling of some conversion-type electrode materials[34–36]. The electrochemical

reduction of NYZC to Zr and Y to their metallic state is in agreement with reported computational work[37]. The reduction of Zr or Y to the metallic state has also previously been observed in Li solid electrolytes when $Li_7La_3Zr_2O_{12}$ or Li_3YCl_6 was in contact with Li metal, respectively.[38,39] The reduction reaction of NYZC can be written as follows:

$$4\ Na_{2.25}Y_{0.25}Zr_{0.75}Cl_6 + 15\ Na \rightarrow 24\ NaCl + Y + 3\ Zr \qquad \text{Equation (1)}$$

When electrochemically sodiated, the NPS sample showed a new set of peaks in the S 2p region corresponding to Na_2S (Figure 5c). The presence of Na_2S is even more pronounced in the chemically sodiated one (Figure 5d). New signals are observed in the P 2p region of chemically sodiated NPS and are assigned to the presence of Na_3P based on previous computational predictions.[40,41] The presence of Na_2S and Na_3P in chemically sodiated NPS was also confirmed by the use of XRD (Figure 6b), which is in agreement with previous work of Wenzel *et al*.[42] The reduction of NPS into Na_2S and Na_3P is summarized in Equation (2).

$$Na_3PS_4 + 8\ Na \rightarrow 4\ Na_2S + Na_3P \qquad \text{Equation (2)}$$

The NBH electrolyte showed no noticeable change in the B 1s peak position (188.0 eV) for neither the electrochemically nor the chemically sodiated samples (Figure 5e). The boron (B^0) reference exhibits a peak at lower binding energy (187.5 eV), thus indicating that the B in NBH was not reduced to its neutral state. Moreover, the XRD pattern recorded on the chemically sodiated NBH only shows the diffraction peaks of pristine NBH and Na metal (Figure 6c), demonstrating the stability of NBH in strong reductive conditions. The NBH electrolyte contains two different borohydride anions, $[B_{10}H_{10}]^{2-}$ and $[B_{12}H_{12}]^{2-}$, whose structures are constructed based on the covalent heccaidecadeltahedron B_{10} and icosahedron B_{12}, respectively. Each boron vertex is covalently connected to a hydrogen atom and the negative charge is delocalized over the $[B_xH_x]^{2-}$ cages.[43] The hydrogens in $[B_xH_x]^{2-}$ are hydride, bearing a negative charge, which cannot be further

reduced. Moreover, the bonding between boron atoms in the B_{10} and B_{12} polyhedra is highly covalent in nature which cannot be easily broken by any reducing agents. A combination of these two factors offers NBH a significant resistance to reduction even at 0 V vs Na/Na^+.[44–46]

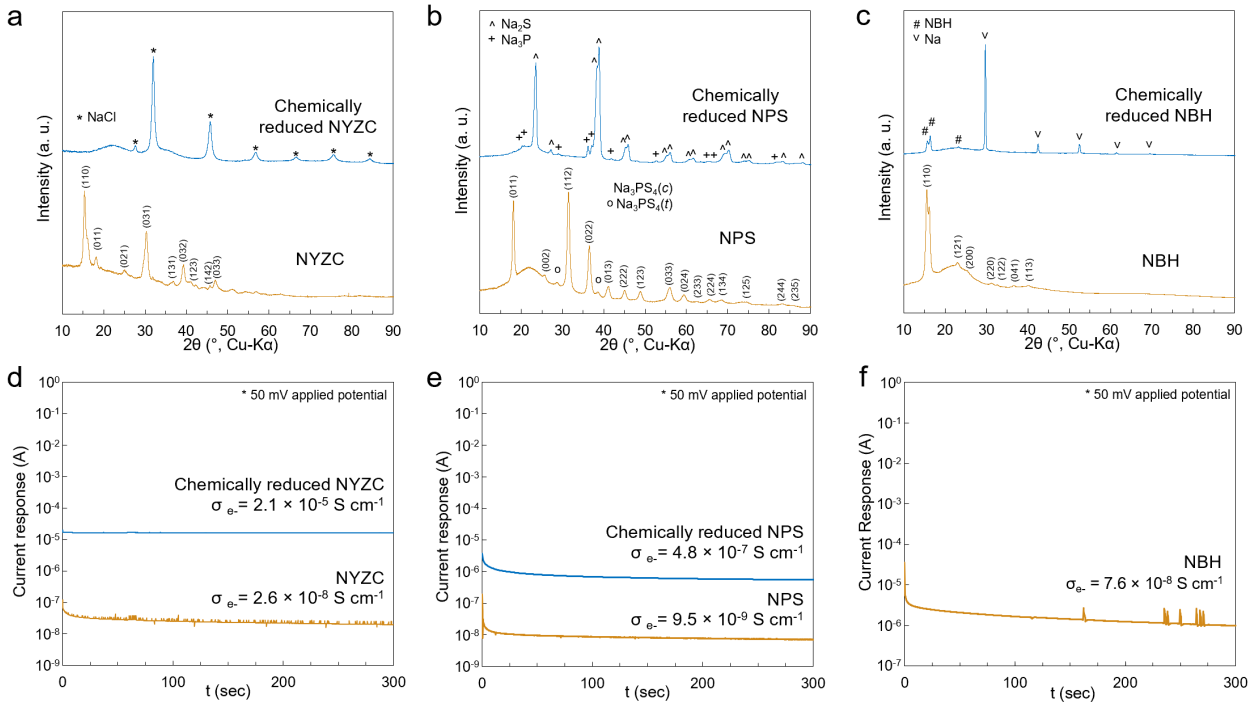

Figure 6. XRD of (a) NYZC, (b) NPS, and (c) NBH after mixing with Na metal and DC polarization electronic conductivity measurements of the reduced (d) NYZC and (e) NPS interphase materials along with (f) pristine NBH.

Discussion

The electrochemical cycling of Na_9Sn_4 | SSE | Sn half cells using NYZC, NPS, and NBH as separator exhibited significantly different behaviors (Figures 3d–f). The cell with NYZC showed instant failure from the first cycle while NPS and NBH exhibited a higher ICE of 66% and 82%, respectively. Furthermore, an interphase layer of 90 μm and 10 μm was observed in the cells using NZYC and NPS as separator while none was detected with NBH (Figures 3g–i). As the

degree of interface passivation depends greatly on the electronic property of the degradation products within the interlayer, DC polarization was performed on the chemically sodiated SSEs to determine their electronic conductivity (Figure 6d).

The reduced NYZC sample exhibited an increase in electronic conductivity by three orders of magnitude compared to the pristine material, which was assigned to the formation of Y and Zr metals (Equation (1) and Figures 5a−b) which are good electron conductors[47]. The formation of an electron conducting layer at the NZYC−Sn interphase induces a rapid and continuous consumption of NYZC and a growth in interlayer thickness (Figure 3g). NaCl was also detected as a degradation product of chemically sodiated NYZC (Figure 6a); however, the ionic conductivity of NaCl is almost negligible at ambient temperature ($\sigma_{Na^+} = 10^{-15}$ S·cm^{-1})[48] , leading to the significant increase in the cell polarization (Figure 4d). NYZC represents the worst-case scenario for an interlayer at the anode side in ASSBs, where the degradation products are electronically conductive and ionically insulating, resulting in a continuous consumption of Na inventory and an excessively high interface impedance. Therefore, this class of SSEs cannot be used with low-voltage anodes even if there is a large excess of Na reservoir in the system.

DC polarization measurements on chemically sodiated NPS showed an increase in electronic conductivity by about two orders of magnitude compared to the pristine material (Figure 6e). As Na_2S in the interlayer is an electronic insulator, the increase in electronic conductivity can be attributed to Na_3P, which was predicted to have a narrow band gap of 0.5 eV[49]. This electronic conductivity increase paired with the known fast Na^+ diffusion in Na_3P[50] indicates that the reduction of NPS results in the formation of an MCI layer, in which Na_3P is the main electronic and ionic conductor. Intuitively, NPS is a prime example of why galvanostatic cycling of symmetric cells are not always a reliable method for evaluating interface stability. As shown in

Supplementary Figure 4**,** the polarization of the cell during plating/stripping remained relatively constant. This would suggest that the interface is stable. However, based on our results presented here, it is known that the interface is not stable. We attribute this counterintuitive result to the mixed-conducting interlayer present after the reduction of NPS. Due to the ionically conductive interlayer, there is minimal change to the cell polarization. In contrast, the interlayer formed from the reduction of NYZC is ionically insulating, resulting in significant cell polarization during plating/stripping cycles (Supplementary Figure 4**)**. Furthermore, the interfacial degradation with NPS is less severe than NZYC (Figure 3h and Figure 4e), which can be explained by the lower electronic conductivity of Na_3P compared to Zr and Y metals. While NPS is commonly used in Na-ASSBs,[23,48] it has always been paired with anodes containing excess Na. Any Na consumed in the MCI formation can be compensated by a nearly unlimited Na reservoir in the anode, which explains the apparent high-capacity retention of reported cells. Based on the data presented here, the use of NPS should be carefully evaluated, particularly when designing commercial full cells in which the separator thickness is reduced to 10-25 μm and the amount of Na in the system is limited.

NBH exhibited superior stability against reduction conditions and no degradation products could be detected in the conditions tested here (Figure 6c). In an electrochemical cell, the NBH−Sn interface is electrochemically stable or at least is passivated by an SEI layer with a negligible thickness (Figures 3i and 4i), allowing for the observed ~99% Coulombic efficiency over long-term cycling (Figure 2d). The reduction stability of NBH is a synergistic effect of the utilization of the hydride anion (H^-) and highly stable boron clusters.

The data presented here highlights the importance of utilizing suitable SSEs to achieve a stable SSE−Anode interface to ensure a stable long-term cycling in Na-ASSBs. No anolyte was utilized in all the cell architectures in this study, and thus the interfacial degradation was limited

to the 2D contact between the Sn anode and SSE separator, which is effectively the least severe scenario. In a practical cell design, a composite anode with a higher contact area between SSEs and Sn may be employed, and any interfacial degradation will be intensified or accelerated. Nonetheless, the information accumulated in this work points out some important future directions for SSE selection and design to achieve a stable SSE−Anode interface; as the SSE is subjected to reductive potentials when it is in direct contact with the anode, an ideal SSE at the SSE−Anode interface should be completely stable against all reduction conditions or at least able to form an ionically conductive and electronically insulating passivation layer.

Beyond the first few cycles in which the interlayers are expected to form, some capacity fade was still observed during later cycles using NPS or NBH separator. FIB milling was conducted on the cells after 1000 cycles (Supplementary Figure 5). The morphology of the Sn and interphase layers in the Sn | NPS | NYZC | $NaCrO_2$ cell were similar to that observed in the half cell (Figure 3h) in which an interphase layer was observed at the interface between the Sn anode and NPS electrolyte. Interestingly, the cell using NBH still did not exhibit any noticeable interphase layer even after many cycles (Supplementary Figure 5b). This reiterates the highly stable nature of the NBH material against the reductive environment at the Na_xSn electrode. Sn pulverization was observed in the NBH cell as evidenced by the disconnected Sn particles compared to the dense pristine Sn layer (Figure 3c). This was likely the origin of the observed slow capacity fade, as a loss of electronic contact between the Sn particles and current collector would result in those Sn particles becoming inactive. Sn pulverization can be attributed to the significant amount of volume change that occurs during the (de)sodiation of Sn (420%).[49] Due to the consumption of Na inventory when forming the interphase layers with NYZC and NPS electrolytes, the Sn received less Na and therefore likely did not undergo as much volume change

compared to the NBH cell, which underwent two times more exchanged capacity compared to the NPS during the course of the study. Therefore, a dense Sn layer was still observed after long cycling with NPS as the electrolyte (Supplementary Figure 5a). This data suggests that the main mechanism for capacity fade when using NPS is interlayer formation and consumption of sodium inventory. This can be seen both visually in the cross-sectional imaging and in the Coulombic efficiency data. The low ICE followed by several more cycles of < 99% efficiency is the typical signature of interlayer growth and subsequent passivation. Conversely, the main mechanism for capacity loss when using NBH is not interlayer formation, but rather mechanical pulverization of the Sn electrode due to significant volume change. The Coulombic efficiency data reaches 99% at the second cycle which indicates a stable anode-electrolyte interface after the first cycle. After solving the interface challenges facing Na-ASSBs, by utilizing novel borohydride electrolytes, attention can begin to focus on remaining challenges such as mechanical degradation of the anode, moving the field one step closer to practical sodium-based energy storage systems.

Conclusions

Here we characterize the reduction stability of Na solid electrolytes belonging to three different material families: NYZC, NPS, and NBH. The cells using these electrolytes exhibited different interlayer thicknesses and cycling performance. During electrochemical cycling, $Na_{2.25}Y_{0.25}Zr_{0.75}Cl_6$ is reduced to form an electronically conductive and ionically insulating interphase, which propagates rapidly, accelerating capacity loss and increasing cell impedance. The reduction of Na_3PS_4 results in the formation of Na_2S and Na_3P products, which is a mixed-conducting interphase, that may continue to grow after each cycle. Nonetheless, the growth of the NPS MCI layer thickness and cell impedance was less severe compared to $Na_{2.25}Y_{0.25}Zr_{0.75}Cl_6$.

Furthermore, no reduction of $Na_2(B_{10}H_{10})_{0.5}(B_{12}H_{12})_{0.5}$ could be observed under the conditions evaluated here. Cells with $Na_2(B_{10}H_{10})_{0.5}(B_{12}H_{12})_{0.5}$ exhibited the highest first Coulombic efficiencies and capacity retentions, owing to the superior stability of the NBH electrolyte. This study shows the need to move beyond commonly used electrolytes like Na_3PS_4, and to develop new materials that can minimize Na inventory loss and impedance growth to enable practical full cell architectures. Furthermore, it allows us to continue our work attempting to enable an anode-free sodium all-solid-state battery using this newly evaluated NBH material.

Methods

Due to the sensitivity of many solid electrolyte and electrode materials to H_2O and O_2 in air, all experiments were performed inside an Ar-filled glovebox, unless otherwise noted.

Solid-state-electrolyte syntheses. $Na_{2.25}Y_{0.25}Zr_{0.75}Cl_6$ was synthesized by ball-milling a stoichiometric ratio of NaCl (99%, Sigma Aldrich), YCl_3 (99.99%, Sigma Aldrich), and $ZrCl_4$ (99.99%, Sigma Aldrich) according to a previously established procedure. Na_3PS_4 was obtained from a stoichiometric ratio of Na_2S (99%, Nagao) and P_2S_5 (99%, Sigma Aldrich). $Na_2(B_{10}H_{10})_{0.5}(B_{12}H_{12})_{0.5}$ was synthesized by ball milling a stoichiometric ratio of $Na_2B_{10}H_{10}$ (98%, Katchem) and $Na_2B_{12}H_{12}$ (99.5%, Katchem), which both had previously been dried under vacuum at 175°C for 48 h. The as-obtained powder material was then again heated under vacuum at 175°C for 48 h.

Ionic conductivity measurements were performed to determine the ionic conductivity of the obtained electrolyte samples (Supplementary Figure 6). The ionic conductivities of NYZC, NPS, and NBH were 0.0627, 0.185, and 1.8 mS cm^{-1}, respectively.

Synthesis of $NaCrO_2$ and Na_9Sn_4 Electrode Materials. $NaCrO_2$ (NCO) was synthesized from a stoichiometric ratio of Cr_2O_3 (99.97%, Alfa Aesar) and Na_2CO_3 (99.5%, Alfa Aesar). The mixture was pelletized and then calcinated under Ar at 900°C for 10 h before naturally cooled to room temperature. Na_9Sn_4 was synthesized by ball-milling Na metal (99.9%) and Sn powder (99%, 10 μm, Sigma Aldrich) in a 2.25/1 (Na/Sn) ratio. Rietveld refinement confirmed that NCO and Na_9Sn_4 were obtained as pure phase (Supplementary Figure 7).

Preparation of Sn Electrodes. Sn electrodes were prepared by casting Sn slurry, containing Sn and polyvinylidene fluoride (PVDF) in a 99.5/0.5 weight ratio dispersed in N-methyl-2-pyrrolidinone (NMP) solvent, on Al foil. The slurry was dried overnight in a vacuum oven at 80 °C.

Cell Fabrication. Solid-state cells were assembled in a 10 mm polyether ether ketone (PEEK) die with two Ti plungers. 70 mg of the SSE (NYZC, NPS, NBH) was pressed under 370 MPa to form a rigid SSE pellet. The thickness of the resulting SSE separator layers was ~500 μm. The Sn anode and the cathode composite containing $NaCrO_2$, NYZC, and vapor grown carbon fibers (VGCF) in a 11/16/1 weight ratio were added to opposing sides of the SSE pellet. 12 mg of cathode composite was used in all experiments. A thin layer of 25 mg NYZC was added before the addition of cathode composite to ensure that the cathode–SSE interface in all the cells was the same; the difference in cell performance can then be attributed to the anode–SSE interface instability. The architecture of full cells is referred to as Sn | SSE | NYZC | Cathode composite (Figure 2). The assembled cells were pressed again at 370 MPa before electrochemical testing. Similarly, Na_9Sn_4 | SSE | Sn half cells were assembled to further investigate anode–SSE interface in later experiments.

Electrochemical Testing. Galvanostatic cycling of the full-cells was performed between 1.7–3.4 V at a current density of 0.064 mA cm^{-2}. Cycling of the half-cells was performed by sodiating the Sn anode until 95% of its theoretical capacity was reached, using a capacity cutoff. The Sn anode was subsequently desodiated until a 2.0 V cutoff was reached, where the applied current density was 0.16 mA cm^{-2}.

Electrochemical impedance spectroscopy measurements were performed using a Solartron 1260 impedance analyzer. Impedance measurements were collected using an applied AC amplitude of 30 mV over a frequency range of 1 MHz to 1 Hz. Direct current (DC) polarization measurements were collected using the potentiostat of the same instrument, by applying 50 mV and measuring the current response over time. The steady-state current was used to calculate the electronic conductivity values.

Focused Ion Beam Scanning Electron Microscopy. The cells were extracted from the PEEK dies by removing the Ti plungers and inserting a 10 mm metal rod into the Na_9Sn_4 side of the cell. The stacked cell and metal rod were then pressed very slowly to push the pellet out of the top of the PEEK die. The pellet was then mounted onto a carbon tape-covered stub. The sample was then mounted onto an air-tight transfer arm while inside the glovebox and sealed. The sample was then transferred into a FEI Scios Dualbeam (ThermoFisher Scientific) chamber without any air-exposure during the transfer. A Ga^+ source was used for ion-beam milling at 30kV and 63 nA. Afterwards, the sample cross-section was cleaned with Ga^+ at 30kV and 15nA. All the imaging was performed with the electron beam source at 5kV and 0.1 nA. EDS mapping was collected using a 10 keV electron beam with a current of 0.1 nA.

X-ray Photoelectron Spectroscopy. XPS measurements were performed using a Kratos Axis Supra XPS instrument. Al Kα radiation was used, and the chamber pressure was less than 5×10^{-8} torr during operation. A charge neutralizer was used for insulating samples and the scan resolution was 0.1 eV with a dwell time of 100 ms. CasaXPS was used for data analysis. The data was calibrated based on the C 1s peak at 285 eV and a Shirley-type background was used.

X-ray Diffraction. XRD measurements were performed using a Bruker APEX II Ultra diffractometer with Mo-Kα (λ=0.7093Å) radiation at 40 kV and 40 mA or a Bruker 3 circle diffractometer with Cu-Kα (λ=1.5406Å) radiation at 45 kV and 50 mA, on flame-sealed boron-rich glass capillaries in a Debye-Scherrer geometry. The diffraction images gathered by the 2D detector within an angular range of 5°-40° for Mo source and range of 10°-90° for Cu source were merged and integrated with DIFFRAC.EVA (Bruker, 2018) to produce 2d-plots. Rietveld refinement was performed using the FullProf software suite.

Acknowledgements

Chapter 1, in part, is a reprint of the material as it appears in Evaluating Electrolyte–Anode Interface Stability in Sodium All-Solid-State Batteries. Deysher, Grayson; Chen, Yu-Ting; Sayahpour, Baharak; Lin, Sharon Wan-Hsuan; Ham, So-Yeon; Ridley, Phillip; Cronk, Ashley; Tan, Darren H. S.; Doux, Jean-Marie; Oh, Jin An Sam; Jang, Jihyun; Nguyen, Long Hoang Bao; Meng, Ying Shirley, ACS Applied Materials and Interfaces, 2022. The dissertation author was the primary author of this paper. Funding to support this work was provided by the National Science Foundation through the Partnerships for Innovation (PFI) grant no. 2044465. Additional support

was provided by the National Science Foundation through the Future Manufacturing (FM) grant no. 2134764. This work was performed in part at the San Diego Nanotechnology Infrastructure (SDNI) of UCSD, a member of the National Nanotechnology Coordinated Infrastructure, which is supported by the National Science Foundation (grant ECCS-2025752). The authors acknowledge the use of facilities and instrumentation at the UC Irvine Materials Research Institute (IMRI), which is supported in part by the National Science Foundation through the UC Irvine Materials Research Science and Engineering Center (DMR-2011967). Specifically, the XPS work was performed using instrumentation funded in part by the National Science Foundation Major Research Instrumentation Program under grant no. CHE-1338173.

Electrochemically Stable Electrolyte

To solve the electrochemical instability previously exhibited when using NPS electrolyte, a sodium borohydride solid electrolyte ($Na_4B_{10}H_{10}B_{12}H_{12}$ (NBH)) was used as the separator (Supplementary Figure 9). NBH has previously been shown to be electrochemically stable against sodium metal [55,56]. Sodium was again electrochemically plated onto the aluminum foil and then stripped away, resulting in a higher ICE of 64% (Figure 7a). This demonstrates the importance of using an electrochemically stable solid electrolyte in anode-free cells. However, the efficiency when using NBH remained unacceptably low, therefore other aspects of the anode-free architecture require improvement.

Intimate Interface Contact

Metal foils are by far the most common current collectors used in batteries, however only a small area of the foil was plated with sodium (Figure 7a), which was confirmed to be metallic sodium by XRD (Supplementary Figure 10). This indicates that there is not sufficient solid-solid contact between the solid electrolyte and the aluminum foil current collector as sodium can only deposit where there is a connection between the incoming Na^+ from the solid-state electrolyte and the electron from the current collector. After stripping, sodium was still observed on the foil, thus explaining the relatively low ICE (Figure 7a). This can be attributed to poor interface contact between the solid electrolyte, sodium metal, and foil current collector which resulted in incomplete stripping of the sodium. This indicates that conventional aluminum foil does not meet the intimate interface contact requirement, resulting in poor reversibility.

To improve the solid-solid interfacial contact between the solid electrolyte and current collector, pelletized aluminum was pressed onto the solid electrolyte separator during cell fabrication in the same process as when using aluminum foil (Figure 7b). Aluminum powder can easily conform to the variable topography of the solid electrolyte separator layer which is formed during the cell fabrication process (Figure 7c). This current collector will be referred to as aluminum pellet. When cycled under the same conditions, the half-cell ICE was significantly improved to 93%. Additionally, a variety of aluminum particle sizes were evaluated and exhibited similar ICE values (Supplementary Figure 11).

When cells were disassembled after plating and after one full cycle, the uniformity of the sodium metal distribution on the current collector surface was found to be greatly improved. Even after plating 1 $mAh{\cdot}cm^{-2}$, which theoretically amounts to an 8.5 μm Na metal layer, the deposition was already uniformly distributed. This implies that the aluminum powder can form a more uniform and intimate contact with the solid electrolyte separator across the entire cell area compared to traditional aluminum foil. This was further demonstrated with electrochemical impedance spectroscopy which showed a lower interfacial resistance when using the aluminum pellet current collector (Figure 7d). Furthermore, the aluminum pellet was shown to evenly distribute the applied stack pressure across the entire area of the cell which was found by inserting pressure-sensitive paper in between the current collector and solid electrolyte layers during cell fabrication (Figure 7e). This likely also helps in uniformly spreading the soft sodium metal as it is plated in cells under stack pressures (10 MPa stack pressure used for this study) well above the yield strength of sodium (~0.2 MPa) [57].

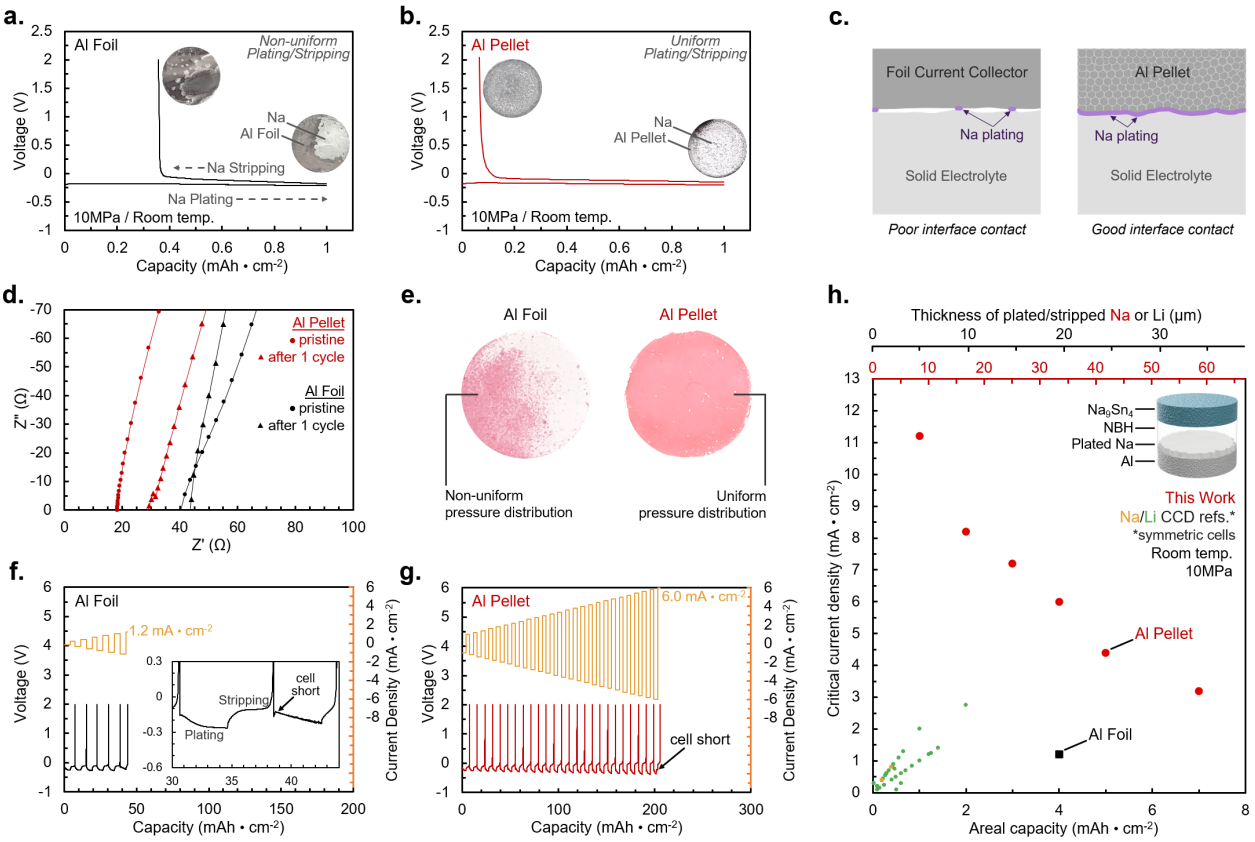

Figure 7. Al pellet comparison with Al foil. Plating/stripping behavior at 1 mA•cm^{-2} current density for a) Al foil and b) Al Pellet current collectors. c) Schematic illustrating the ability of aluminum powder to form intimate contact with the solid electrolyte layer. d) Impedance measurements before and after cycling Al foil and Al pellet cells. e) Pressure paper showing the distribution of pressure over the cell area when using Al foil and Al pellet current collectors. Critical current density when cycling 4 mAh•cm^{-2} capacity with f) Al foil and g) Al pellet current collectors. h) Critical current density (CCD) evaluation as a function of areal capacity at room temperature when using an Al pellet current collector. Cycling data can be found in Supplementary Figure 12. Literature data that utilized cold-pressed solid electrolytes is added for comparison [58–80]. All cycling data in this figure was obtained at room temperature under 10 MPa stack pressure.

Due to the improved contact and sodium plating uniformity, the applied current will be distributed over a larger area compared to when using aluminum foil. As high current density promotes the formation of dendrites [81–83], which can lead to cell short-circuiting, lowering the local current density enables cell cycling at higher total currents. When using aluminum foil and cycling with 4 mAh•cm^{-2} capacity between the electrodes, the critical current density was found to be 1.2 mA•cm^{-2} (Figure 7f). The cell failed during the sodium plating step, and the Na_9Sn_4 counter

electrode was found to cycle at much higher currents (Supplementary Figure 13) therefore this critical current density can be attributed to failure by sodium dendrite penetration through the electrolyte during plating. When using the aluminum pellet current collector, the critical current density increased to 6.0 $mA \cdot cm^{-2}$ (Figure 7g). Interestingly, compared to previously reported critical current density values for cold pressed cells (Figure 7h) our data shows successful cycling at significantly higher currents, even when using an aluminum foil current collector. Most previously reported critical current density values are ≤ 2 $mA \cdot cm^{-2}$ at ≤ 2 $mAh \cdot cm^{-2}$ capacity. This indicates that there may be another factor governing the high current ability of these cells, besides the type of current collector.

Dense Solid Electrolyte

Anode-free cells rely on the nature of the interface between the current collector and the solid electrolyte. Therefore, the solid electrolyte properties are also important to consider when assessing this type of cell architecture. Focused-ion beam milling scanning electron microscopy (FIB-SEM) was used to evaluate the morphology of the NBH solid electrolyte after cold pressing to form the separator layer (Figure 8a-c). The NBH electrolyte separator exhibited an extremely dense morphology. The crosshatch line pattern textured on the surface is due to the imperfect titanium plunger used to press the solid electrolyte layer (Supplementary Figure 14). More importantly, only a few rounded micron-sized surface pores were observed indicating good compaction without the need for high temperature sintering (Figure 8b). The cross-section of the NBH was intentionally milled at the spot of one of the surface pores to examine how deep they protrude into the electrolyte layer. It was found that the pores have a rounded morphology that does not extend further than ~1 μm (Figure 8c). In addition to the intimate interface contact

achieved by using the aluminum pellet current collector, the dense morphology of NBH also contributes to the observed high critical current densities. It is known that imperfections in the solid electrolyte separator such as pores and cracks can result in dendrite penetration and cell short circuiting [27–31]. Without these imperfections, it becomes much more difficult for sodium to penetrate the solid electrolyte layer (Figure 8d).

To compare with lithium solid electrolytes, $Li_4B_{10}H_{10}B_{12}H_{12}$ (LBH) was selected as a direct comparison with NBH as it has also been shown to achieve an electrochemically stable interface with lithium metal [84]. Li_6PS_5Cl (LPSCl) was also selected due to its common use in lithium solid-state batteries. These solid electrolytes were found to exhibit porous morphologies after cold pressing (Supplementary Figure 15). When these electrolytes were used as the separator in lithium half-cells, the cells short circuited shortly after the plating step began and could only be successfully cycled at much lower current densities (0.1 $mA \cdot cm^{-2}$). This can be attributed to the soft lithium creeping into the surface cracks of the separators [30], which can result in current concentrations at the tips of the lithium metal filaments and further exacerbate the filament growth through the solid electrolyte [85]. NBH materials on the other hand have been shown to be softer than their lithium counterparts [86], but previously there have been no visual observations of the highly dense morphology that can be achieved by cold pressing when using NBH. The high sodium critical current density can be attributed to this newly revealed ability of this borohydride electrolyte.

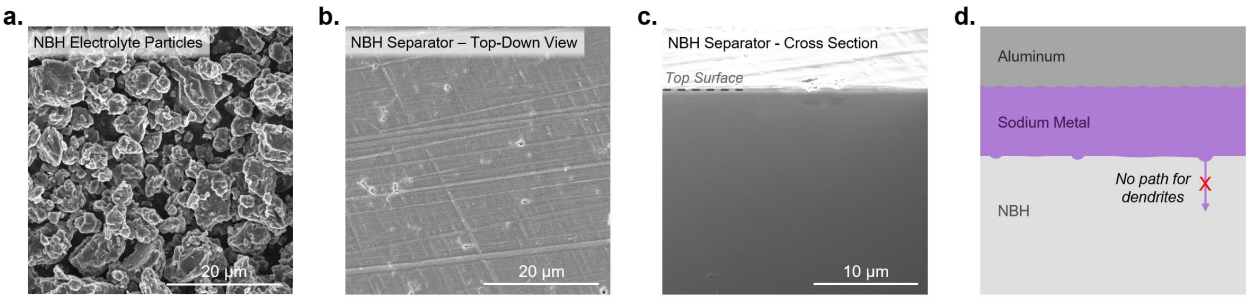

Figure 8. Evaluation of NBH morphology. SEM of a) NBH particles and b) top view of the NBH separator after cold pressing. c) FIB-SEM cross section view of NBH separator. d) Schematic illustrating the propensity of sodium to deposit without forming dendrites through the electrolyte.

Dense Current Collector

To probe the effect of the current collector morphology, aluminum, copper, and titanium were selected for comparison due to their common use in solid-state battery research as current collectors and cell materials. Like aluminum, copper and titanium do not form alloys with sodium, ensuring that they will only act as a current collector [87–89]. Using a half-cell configuration, the plate/strip ICEs were significantly different (Figure 9a-c). There were also small slope regions observed in the voltage curves during the initial stages of plating when using copper and titanium. This is attributed to the surface oxide layers present on these metals that react with the incoming sodium forming an oxide (Supplementary Figure 16). This likely contributes partially to the irreversible capacity due to the high bonding energy between sodium and oxygen although the thin nature of the surface oxides and the small capacity observed within the slope regions indicates that it is not the major factor affecting the overall irreversibility.

After repeated cycling the aluminum cells exhibited the highest capacity retention followed by copper, and then titanium which had the lowest capacity retention (Figure 9d). As the solid electrolyte-current collector interface is known to play a critical role in the cyclability of solid-state anode-free cells (Figure 7), the surface topography of the three current collectors was compared using optical profilometry (Figure 9e-g). While all three current collectors exhibited

slightly different surface textures, likely correlated to their powder morphology (Supplementary Figure 17), the roughness of their surfaces were close in value; 0.98 µm, 1.05 µm, and 0.90 µm for aluminum, copper, and titanium respectively. Therefore, their degree of contact with the solid electrolyte separator should be similar. This indicates that the reversibility differences may be due to a bulk current collector effect rather than an interface variation.

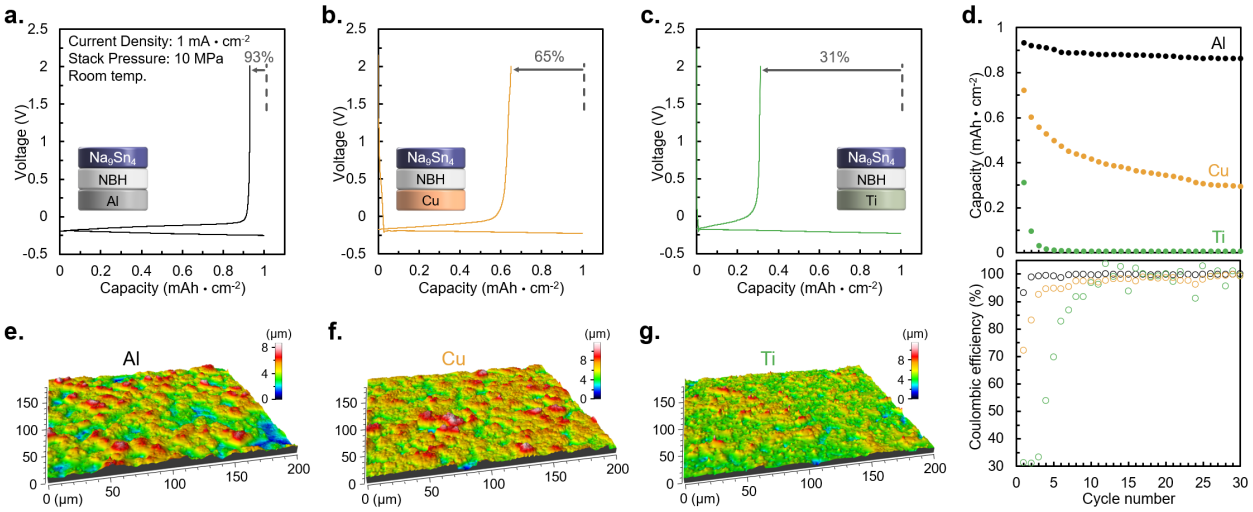

Figure 9. Evaluation of various pelletized current collectors. First cycle plating/stripping voltage curves of half-cells using a) Al, b) Cu, and c) Ti pellet current collectors. d) Electrochemical performance of the same three cells over 30 cycles. Optical profilometry measurements of the surface topography of e) Al, f) Cu, and g) Ti pellet current collectors. All cycling data in this figure was obtained at room temperature under 10 MPa stack pressure with a current density of 1 mA•cm^{-2}.

To evaluate the bulk morphology of the three current collectors, FIB-SEM was used to image their cross-sections. As shown in Figure 10a-c, the aluminum current collector was almost fully dense. By using the weight and volume of the pellet, the porosity of the aluminum was calculated to be 0 – 3%. In contrast, the copper current collector contained many micron-sized pores (19 – 23% porosity), and similarly, the titanium current collector contained many larger pores (34 – 35% porosity). To establish a quantitative trend comparison between these three

materials, several current collectors were fabricated at various pressures and their porosities were determined (Figure 10d). It was found that aluminum powder can densify more easily than copper and titanium powders which can be explained by the varying mechanical properties of these three materials in which aluminum possesses the lowest Vickers hardness (~160 MPa) compared to copper (~370 MPa) and titanium (~970 MPa) [90].

To evaluate the potential impact of the current collector porosity on the reversibility of sodium plating/stripping, FIB-SEM was used again on cycled cells after one plate/strip cycle. These results (Figure 10e-g) show that when pores are present in the current collector, sodium metal can become trapped inside during plating. Since there is no liquid electrolyte present and the solid electrolyte separator is unable to flow into the current collector pores, the sodium in the pores becomes ionically insulated after the sodium metal at the solid electrolyte-current collector interface is stripped away (Figure 10h). This results in a sodium trapping effect which can be seen in the sodium energy dispersive X-ray spectroscopy (EDS) maps (Figure 10e-g). Therefore, the use of aluminum was found to be critical to enable reversible plating/stripping, as it is soft enough to become highly dense after cold pressing during cell fabrication.

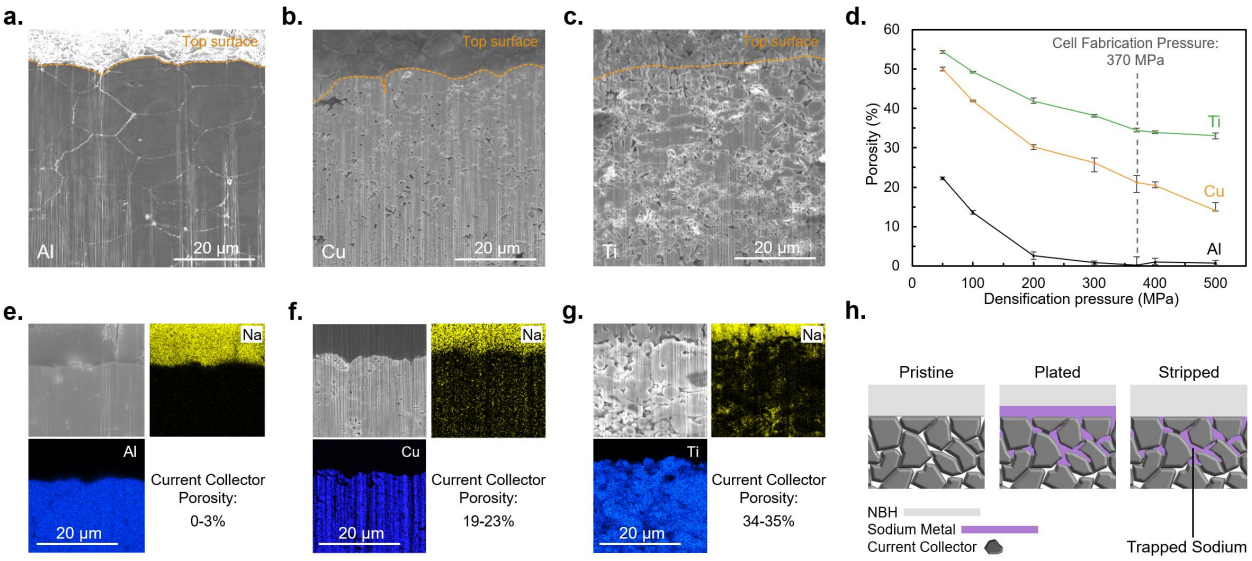

Figure 10. Evaluation of pelletized current collector morphologies. FIB-SEM cross section views of pristine a) Al, b) Cu, and c) Ti pellet current collectors. d) Current collector porosity as a function of fabrication pressure. FIB-SEM cross section views of e) Al, f) Cu, and g) Ti current collectors after one plate/strip cycle with EDS mapping. h) Schematic of Na trapping mechanism for porous current collectors.

Stack Pressure and Sodium Morphology

Beyond enabling reversible cycling in an anode-free architecture, there are other important practical cell performance considerations to evaluate. Often, high stack pressures (50 – 250 MPa) are used for solid-state cell cycling [30,91–95]. This is not a commercially viable option because larger area cells, such as 3×3 cm^2, can require forces exceeding 10 tonnes (Figure 11c). It is likely that no battery pack casing will be able to achieve such high pressures safely and consistently without using a heavy construction and thus lowering the cell energy density. Instead, lower pressure cycling should become the norm for solid-state battery research. Due to their low moduli, bulk alkali metal anodes are known to work well at lower pressures [96,97]. To assess the effect of cell stack pressure on cyclability in this anode-free cell configuration, half-cells were cycled at 5, 10, 15, and 20 MPa of constant stack pressure (Figure 11a-b). When 10 – 20 MPa was used, the cells

exhibited very similar reversibility and capacity retention. This indicates that pressures higher than 10 MPa are not needed. 5 MPa cycling was found to be less reversible. As no noticeable difference in the cyclability of Na_9Sn_4 was observed at 5 and 10 MPa (Supplementary Figure 13), the change in anode-free half-cell performance at 5 MPa can be attributed to the anode-free side. The lower reversibility of anode-free cycling at 5 MPa can be attributed to the difficulty in maintaining intimate solid-solid contact between the current collector, sodium metal, and solid electrolyte which is essential for complete stripping of the deposited sodium. Currently, this is a common limitation for solid-state batteries due to the difficulty in maintaining intimate contact between solid materials. Stack pressure requirements may require heavier battery pack casings which can limit the overall system energy density and increase the cost. As such, it is important for future research to focus on finding ways to lower the required stack pressure. One method may be the use of elevated temperatures. Lower pressures such as 5 and 1 MPa can be enabled using a slightly elevated cycling temperature (Supplementary Figure 18). At 40 °C, the efficiency of 5 and 1 MPa cells became similar to that of 10 MPa presumably due to the softening of metallic sodium [98], which can facilitate the retention of intimate solid-solid interfaces even at lower pressures.

Areal capacity is also important to consider as higher areal capacities result in higher overall energy densities by maximizing the active: inactive material ratio. Using 10 MPa stack pressure, it was found that cycling 1, 3, and 7 $mAh \cdot cm^{-2}$ capacity of sodium, corresponding to 8.8, 26.5, and 61.9 μm of deposited sodium respectively, exhibited very similar reversibility and capacity retention (Figure 11d-e). Furthermore, similar plating/stripping efficiencies were observed for both 10- and 13-mm diameter cells, which indicates that larger cell areas are also possible (Supplementary Figure 19). Lastly, an anode-free half-cell was found to exhibit a high Coulombic efficiency for 1000 cycles (Supplementary Figure 20). The sodium morphology and

NBH interface conformity was evaluated using cryogenic FIB-SEM (Figure 11f) and EDS mapping (Supplementary Figure 21). The aluminum interface conformity was also evaluated. The sodium was found to form a dense and intimate interface with both the NBH and the Al which is critical for enabling sufficient ion and electron transfer respectively.

To evaluate the bulk sodium morphology after plating, a cell was examined using cryo-FIB-SEM after plating 7 mAh•cm^{-2} capacity (Figure 11g). The electrochemically deposited sodium metal contained no pores in the area examined. This dense morphology is unique to this solid-state cell architecture under stack pressure compared to the mossy sodium observed when using liquid electrolytes at very low pressures. To evaluate the sodium morphology over a larger scale, an X-ray computed tomography scan was performed on a smaller 4 mm diameter cell after plating 7 mAh•cm^{-2} capacity (Figure 11h). The sodium was found to be uniformly distributed across the surface of the current collector (Figure 11i) and no significant morphological features were observed. This can be attributed to the homogenous plating of sodium due to the intimate and electrochemically stable interface which is responsible for enabling the highly efficient plating/stripping observed for areal capacities as high as 7 mAh•cm^{-2}.

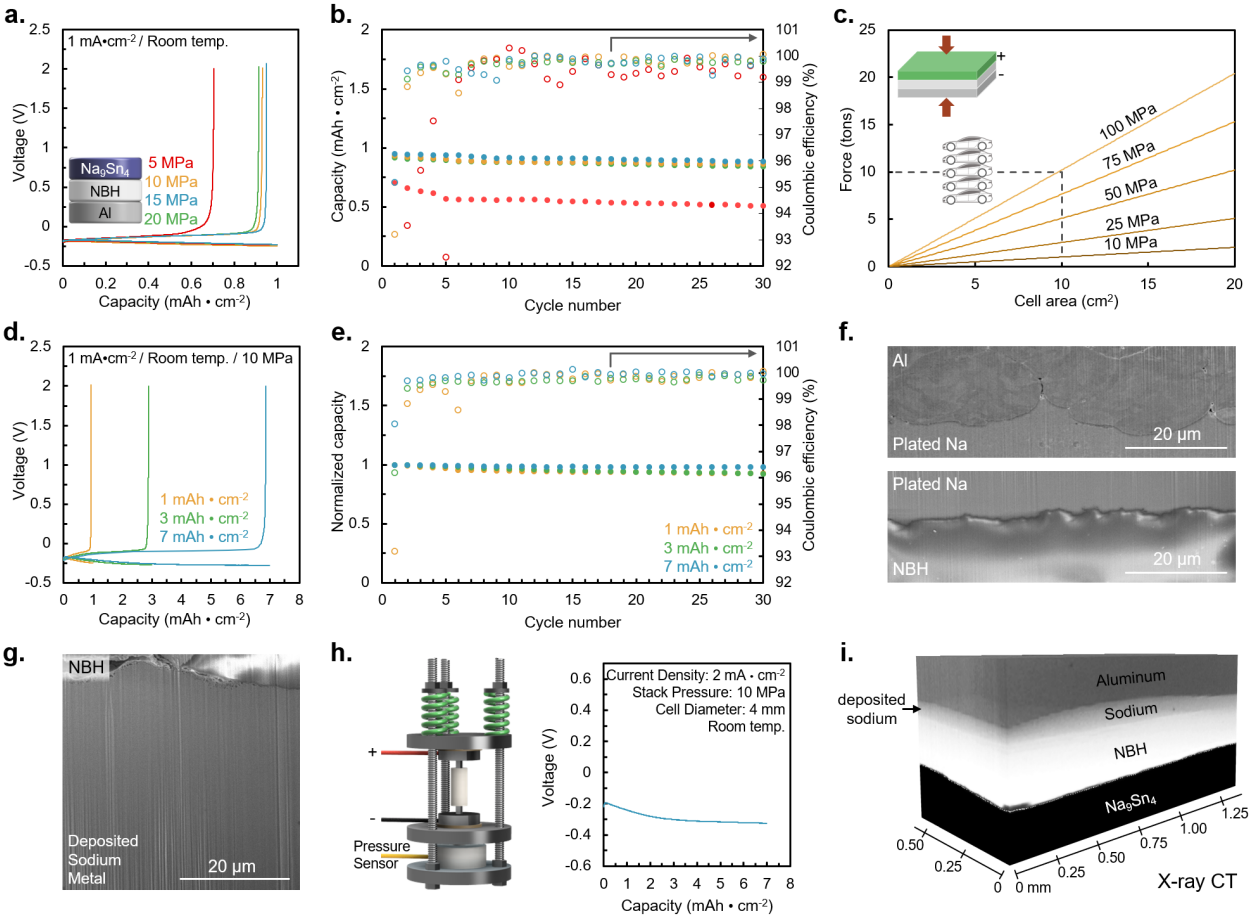

Figure 11. Effects of cell stack pressure and areal capacity. a) Voltage profiles for Na_9Sn_4 | NBH | Al half-cells cycled at 5, 10, 15, and 20 MPa. b) Capacity retention during extended cycling of the same cells. c) Force required to achieve various stack pressures. d) Voltage profiles for Na_9Sn_4 | NBH | Al half-cells cycled with 1, 3, and 7 mAh•cm^{-2} capacities. e) Capacity retention during extended cycling of the same cells. Cryo-FIB/SEM images of the f) Na-Al and Na-NBH interfaces and g) thick plated sodium. h) Cell holder schematic and cycling data for a custom 4 mm diameter X-ray computed tomography cell. i) X-ray computed tomography scan of 7 mAh•cm^{-2} plated sodium metal. All cycling data in this figure was obtained at room temperature.

Anode-Free Sodium All-Solid-State Full-Cell

To demonstrate an anode-free sodium all-solid-state full-cell, a low cost $NaCrO_2$ cathode was used and paired with a $Na_{0.625}Y_{0.25}Zr_{0.75}Cl_{4.375}$ catholyte (Supplementary Figure 22) that is known to be electrochemically stable against $NaCrO_2$ [99]. When cycled at room temperature, the cell experienced noticeable polarization (Figure 12a). To overcome the slow cathode kinetics, the

full-cell was cycled at a higher temperature of 40 °C (Figure 12b). This improved the cathode capacity utilization at higher currents (Figure 12c). Additionally, a constant voltage hold can be added at the charged state to maximize the extraction of capacity from the cathode. With this protocol, the ICE of 93% was achieved which is similar to the ICE achieved in anode-free half cells (Figure 12d). The cell maintained stable cycling for 400 cycles with a capacity retention of 70% (Figure 12e) which is due to the high average Coulombic efficiency of 99.96% achieved under these cycling conditions (10 MPa, 40 °C). This performance is attributed to the combination of the aluminum pellet current collector with the sodium borohydride solid electrolyte. This demonstrates the significant improvement when using an aluminum pellet compared to conventional aluminum foil which can only cycle for tens of cycles before losing most of its capacity (Figure 12f). While the aluminum pellet current collector used in this study is several hundred microns thick (Supplementary Figure 23), reducing the thickness may be possible by using a thin layer of aluminum particles cast onto aluminum foil followed by a transfer process (Supplementary Figure 24). Furthermore, although higher cathode loadings and thinner solid electrolyte layers will be needed to enable the full potential of this cell architecture, this truly anode-free cell design demonstrates the effectiveness of dense solid electrolyte and current collector morphologies as well as a robust interface between them.

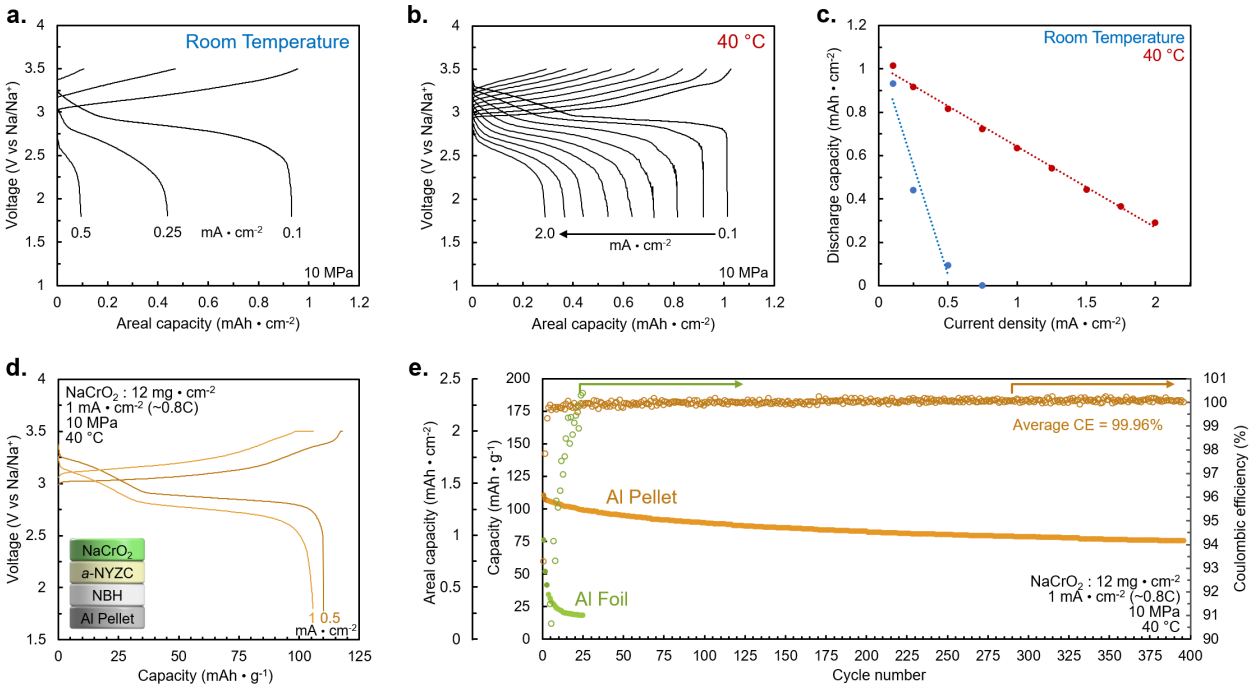

Figure 12. Anode-free sodium all-solid-state full-cell cycling. Voltage curves of a sodium anode-free half-cell cycled at various currents at a) room temperature and b) 40 °C. Voltage curves for the first three formation cycles are not shown. c) Cathode capacity as a function of current density. d) Voltage curves of a sodium anode-free solid-state full-cell including a constant voltage hold at 3.5 V and e) cell capacity over 400 cycles for the same cell combined with Al foil data for comparison. Energy efficiency data is provided in Supplementary Figure 25. A comparison with Na_9Sn_4 anode is included in Supplementary Figure 26. $NaCrO_2$ cathode was used in all cells. All cycling data in this figure was obtained under 10 MPa stack pressure.

Conclusion

In this work we enable stable cycling in an anode-free all-solid-state battery architecture which can potentially lead to a significant increase in energy density. A pelletized aluminum current collector was shown to enable improved solid-solid interface contact with the borohydride-based solid electrolyte. This intimate interface enabled significantly higher current density cycling. By pairing the dense aluminum pellet current collector with a sodium borohydride solid electrolyte, reversible cycling was achieved for capacities as high as 7 mAh•cm^{-2} (62 µm of sodium) due to the electrochemically stable and dense solid electrolyte combined with the

application of 10 MPa stack pressure. Using a low-cost $NaCrO_2$ cathode, an anode-free sodium all-solid-state full-cell battery was demonstrated to cycle several hundred cycles. This work elucidates the four critical factors that govern the electrochemical performance of anode-free solid-state cell designs to guide future developments of high energy all-solid-state batteries. We believe that this work can guide the discovery and implementation of other anode-free battery chemistries and serve as an example that sodium can compete with and complement traditional lithium-ion batteries.

Methods

All experiments were conducted in an argon-filled glovebox with oxygen and water levels <5 and <1 ppm respectively.

Material Synthesis –

Zirconia-lined ball milling jars used for synthesis were airtight and sealed inside the glovebox before transferring out onto the ball mill.

$NaCrO_2$. $NaCrO_2$ was synthesized by mixing a stoichiometric amount of Na_2CO_3 (99.5%, Alfa Aesar) and Cr_2O_3 (99.97%, Alfa Aesar) with a mortar and pestle. This 1 g mixture was then pelletized under 370 MPa and then heated in a tube furnace under flowing argon at 5 °C • min^{-1} to 900 °C and held for 10 h before ambient cooling to room temperature (~ 5 h). XRD data for the obtained material is shown in Supplementary Figure 27.

Na_9Sn_4. Na_9Sn_4 was synthesized by mixing a stoichiometric amount of Na metal (99.8%, Sigma Aldrich) with Sn powder (10 μm, 99%, Sigma Aldrich) with a mortar and pestle. The 1 g mixture was then ball milled at 500 rpm for 2 h in a Retsch Emax high energy ball mill. XRD data for the obtained material is shown in Supplementary Figure 28.

$Na_4B_{10}H_{10}B_{12}H_{12}$. NBH was synthesized by mixing a stoichiometric amount of $Na_2B_{10}H_{10}$ (Boron Specialties) and $Na_2B_{12}H_{12}$ (Boron Specialties) with a mortar and pestle. This 1 g mixture was then ball milled at 450 rpm for 2 h in a Retsch PM100 planetary ball mill. The resulting material was then dried at 175 °C for 48 h under dynamic vacuum. XRD data for the obtained material is shown in Supplementary Figure 28 and conductivity measurements are shown in Supplementary Figure 9.

$Na_{0.625}Y_{0.25}Zr_{0.75}Cl_{4.375}$. *a*-NYZC was synthesized by mixing a stoichiometric amount of NaCl (99%, anhydrous, Sigma Aldrich), YCl_3 (99.99%, anhydrous, Sigma Aldrich), and $ZrCl_4$ (99.99%, anhydrous, Sigma Aldrich) with a mortar and pestle. The 1 g mixture was then ball milled at 500 rpm for 2.5 h in a Retsch Emax high energy ball mill. The material was removed and homogenized with a mortar and pestle before ball milling for another 2.5 h. XRD data for the obtained material is shown in Supplementary Figure 27 and conductivity measurements are shown in Supplementary Figure 22.

Na_3PS_4. NPS was synthesized by mixing a stoichiometric amount of Na_2S (99%, anhydrous, Nagao) with P_2S_5 (99%, Sigma Aldrich) with a mortar and pestle. This 1 g mixture was then ball milled at 450 rpm for 2 h in a Retsch PM100 planetary ball mill.

$Li_4B_{10}H_{10}B_{12}H_{12}$. LBH was synthesized by mixing a stoichiometric amount of $Li_2B_{10}H_{10}$ (Boron Specialties) and $Li_2B_{12}H_{12}$ (Boron Specialties) with a mortar and pestle. This 1 g mixture was then ball milled at 450 rpm for 2 h in a Retsch PM100 planetary ball mill. The resulting material was then dried at 175 °C for 48 h under dynamic vacuum. The material was then ball milled again for 2 h.

Li_6PS_5Cl. Li_6PS_5Cl was obtained from NEI Corporation.

Li_7Sn_3. Li_7Sn_3 was synthesized by gently mixing a stoichiometric amount of Stabilized Lithium Metal Powder (SLMP) metal (FMC, USA) with Sn powder (10 μm, 99%, Sigma Aldrich) with a mortar and pestle.

Cathode Composite Fabrication. $NaCrO_2$, *a*-NYZC, and vapor grown carbon fibers (98%, Sigma Aldrich), were mixed in a 11:16:1 weight ratio with a mortar and pestle.

Cell Assembly. 50 mg of NBH was pressed between two polished titanium plungers in a 10 mm diameter PEEK die at 100 MPa.

Half-cells. 100 mg of Na_9Sn_4 was added to one side and 200 mg of Al powder (99.97%, -325 mesh, Fisher Scientific), Cu powder (99%, -325 mesh, Fisher Scientific), or Ti powder (93%, < 20 μm, Fisher Scientific) was added to the other side of the NBH. The cells were then pressed at 370 MPa.

Full-cells. 10 mg of *a*-NYZC was added as a protective layer between the NBH separator and the cathode composite. 24 mg of cathode composite was then added on top of the *a*-NYZC layer. When using the Al pellet current collector, 200 mg of Al powder was then added to the other side of the NBH. When using Al foil, a 10 mm diameter circle of Al foil was added to the other side of the NBH. The cell was then pressed at 370 MPa.

Cell Cycling. Cells were mounted in clamps containing a pressure sensor and springs to maintain a known and constant pressure during cycling. Unless otherwise noted, cells were cycled under 10 MPa constant pressure at room temperature.

Critical Current Density Measurements. Various cells were evaluated by cycling various fixed capacities of sodium between the electrodes and the current density was increased stepwise after each cycle by 0.2 mA • cm^{-2}. The critical current density was assessed to be the current density at which the cell exhibited short circuit behavior (sudden drop and fluctuating of potential).

Capacity Retention in Half-cells. A certain fixed capacity of sodium was plated onto the anode-free electrode. The sodium was then stripped away to a 2 V cutoff. In the next cycle, the amount of sodium plating was set to the amount of sodium stripped during the previous cycle. For example, if 1 mAh • cm^{-2} was plated and 0.95 mAh • cm^{-2} was able to be stripped, then in the next cycle 0.95 mAh • cm^{-2} was plated. This was done to model the capacity retention of anode-free full-cells, assuming that the cathode is 100% efficient.

Anode-Free Full-Cell. The anode-free full-cell was cycled using 3.5 and 1.8 V upper and lower voltage cutoffs respectively. 3 formation cycles at 0.5 mA • cm^{-2} were done before switching to 1 mA • cm^{-2}. A constant voltage step was added to the end of the constant current charge step to obtain more capacity from the cathode due to cathode kinetic limitations within the sodium cathode composite. The constant voltage was held at 3.5 V until the current reached a value < 0.2 mA • cm^{-2}. Cycling was conducted at 40 °C.

Electrochemical Measurements

Electrochemical Impedance Spectroscopy. EIS measurements were done using a Solartron 1260 impedance analyzer. A frequency range of 1 MHz to 1 Hz was used with an applied AC amplitude of 30 mV. To evaluate solid electrolyte ionic conductivity, 70 mg of solid electrolyte was pressed at 370 MPa between two titanium plungers in a 10 mm diameter PEEK die. 5 mg of acetylene black carbon was added to each side of the electrolyte pellet and the cell was pressed again at 370 MPa. Carbon was added to improve the physical contact between the sample and the electrodes to minimize the interface resistance and obtain a more accurate electrolyte conductivity value.

Direct Current Polarization. The same cell used for EIS was used for polarization measurements. A 50 mV potential was applied to the cell and the current response was measured as a function of time. The current value after 300 sec was used to calculate the electronic conductivity of the solid electrolytes.

Linear Sweep Voltammetry. 9 mg of solid electrolyte and 21 mg of stainless-steel powder was mixed with a mortar and pestle. 70 mg of solid electrolyte was pressed at 370 MPa between two

titanium plungers in a 10 mm diameter PEEK die. 50 mg of Na_9Sn_4 was added to one side of the solid electrolyte and 20 mg of the solid electrolyte/steel mixture was added to the other side. The cell was pressed again at 370 MPa. Two cells were fabricated for each solid electrolyte. One cell was swept to low potential and the other cell was swept to high potential at a rate of 0.1 $mV \cdot s^{-1}$.

Optical Profilometry. A Filmetrics Profilm3D Optical Profiler was used for measurements. A 50x objective lens, white light interferometry, an envelope peak/center setting, and 30 μm scan length were used. Data was analyzed using the profilmonline web-based software.

Focused Ion Beam / Scanning Electron Microscopy –

Ga^+ Ion Source. An FEI Scios Dualbeam FIB/SEM was used. Sample milling was conducted at 30 kV with a 65 nA current. After the initial removal of material, a lower current (7 nA) was used to clean the cross-section surface. Electron imaging was conducted at 5 kV and 0.1 nA beam conditions. An air-tight transfer arm was used to avoid sample exposure to air. The Ga^+ source machine was used for Fig. 3c, 6f, and fig. S7. For sodium metal milling, a liquid nitrogen cooled cryo stage was used.

Xe^+ Plasma Source. A Helios G4 PFIB UXe DualBeam FIB/SEM was used. Sample milling was conducted at 30 kV with a 2.5 μA current. After the initial removal of material, lower currents (500 and 60 nA) were used to clean the cross-section surface. Electron imaging was conducted at 5 kV and 0.4 nA beam conditions. The Xe^+ source machine was used for the Al, Cu, and Ti current collector samples in Fig. 5.

Scanning/Transmission Electron Microscopy. TEM images of Al, Cu, and Ti particle surface were obtained using a Thermofisher Talos F200X G2, equipped with a Ceta camera and operated at 200 kV. S/TEM-EDS was collected using 4 in-column SDD Super-X detectors.

X-ray Photoelectron Spectroscopy. A Kratos Axis Supra instrument utilizing Al kα radiation was used for XPS measurements. The sample chamber pressure was $< 5 \cdot 10^{-8}$ Torr. A dwell time of 100 ms, 0.1 eV scan resolution, and a charge neutralizer was used for measurements. Etching was conducted using argon plasma at time intervals of 5 min to probe the chemical composition of the sample surface as a function of depth. Data analysis was performed using CasaXPS software and the carbon 1s peak was used for calibration. A Shirley-type background was used.

X-ray Diffraction. A Bruker APEX II Ultra diffractometer was used for diffraction measurements. A molybdenum X-ray source (Kα-λ = 0.7093 Å) was used at 40 kV and 40 mA. Flame-sealed boron-rich glass capillaries were used due to the air sensitivity of the materials. A 2D detector collected the diffraction data within an angular range of 5–40° and the data was merged and integrated with DIFFRAC.EVA (Bruker, 2018) to produce 2D patterns. Rietveld refinement was performed using the FullProf software suite. XRD data for plated sodium was obtained by delaminating a half cell and sealing the surface of the exposed sodium with Kapton tape before obtaining the measurement using a Rigaku Miniflex diffractometer with Cu radiation.

X-ray Computed Tomography. A 4 mm diameter cell design was used for CT measurements. A half-cell configuration (Na_9Sn_4-NBH-Al) was used. Using a Versa 510 (Zeiss/Xradia) X-ray microscope a 360° scan was obtained. A 10 s exposure setting, 80 kV source voltage, and 7 W

power were used for the measurements with the objective of 4X without additional filter. The FOV of 2.24 mm x 2.24 mm with a voxel size of 2.22 μm was achieved. Amira 2019.1 software was used for data reconstruction.

Scanning Electron Microscopy. SEM micrographs were obtained with a FEI Apreo instrument. A 5 keV accelerating voltage, 0.1 nA current, and ETD detector were used.

Acknowledgements

Chapter 2, in part, is a reprint of the material as it appears in An Anode-Free Sodium All-Solid-State Battery. Deysher, Grayson; Oh, Jin An Sam; Chen, Yu-Ting; Sayahpour, Baharak; Ham, So-Yeon; Cheng, Diyi; Ridley, Phillip; Cronk, Ashley; Lin, Sharon Wan-Hsuan; Qian, Kun; Nguyen, Long Hoang Bao; Jang, Jihyun; Meng, Ying Shirley, Nature Energy, 2024. The dissertation author was the primary author of this paper. Funding to support this work was provided by the National Science Foundation through the Partnerships for Innovation (PFI) grant no. 2044465 received by Y. S. M. This work was performed in part at the San Diego Nanotechnology Infrastructure (SDNI) of UCSD, a member of the National Nanotechnology Coordinated Infrastructure, which is supported by the National Science Foundation (grant ECCS-2025752). The authors acknowledge the use of facilities and instrumentation at the UC Irvine Materials Research Institute (IMRI), which is supported in part by the National Science Foundation through the UC Irvine Materials Research Science and Engineering Center (DMR-2011967). Specifically, the XPS work was performed using instrumentation funded in part by the National Science Foundation Major Research Instrumentation Program under grant no. CHE-1338173. Xe plasma

FIB experiments were conducted at the University of Southern California in the Core Center of Excellence in Nano Imaging. We also acknowledge the use of the UCSD Crystallography Facility.

Chapter 3 Summary and Future Perspectives

As the desire for renewable energy from solar and wind power plants grows, so does the need for energy storage due to the intermittent nature of these power supplies. Sodium solid-state batteries are the most promising solution due to their lower cost and safer operation compared to modern lithium-ion batteries. Additionally, an anode-free cell design can further reduce the cost of the battery due to the elimination of the costs associated with the anode material. However, at the time of this report, there have been zero published research works on this topic, leaving a highly important matter unresolved.

An anode-free sodium all-solid-state battery requires four essential criteria in order to operate reversibly: electrochemically stable solid electrolyte, intimate contact between the solid electrolyte and current collector, a dense solid electrolyte, and a dense current collector. While some other potential systems can achieve one to three of these criteria it has previously been impossible to achieve all four simultaneously. In this research project, due to careful material selection and cell design, these criteria are met through the use of a sodium borohydride solid electrolyte paired with a novel aluminum pellet current collector.

Although Na_3PS_4 solid electrolyte has been commonly used in the past, it was found to be unstable against the anode-free electrode potential. Therefore other electrolyte candidates were explored to try to find one that exhibits better electrochemical stability. The first candidate was $Na_{2.25}Y_{0.25}Zr_{0.75}Cl_6$ solid electrolyte. This material displayed even worse stability than Na_3PS_4 as seen by the thicker interphase layer that forms during cycling. Based on XRD, XPS, and electronic conductivity data, this difference is attributed to the presence of Y and Zr which reduce to their metallic state when in contact with the anode. When this occurs, their metallic nature allows for the continued flow of electrons through the interphase layer which results in the continuous growth

of the interphase layer and loss of cell capacity. P in Na_3PS_4 was also found to fully reduce however unlink Y and Zr that are metallic conductors, Na_3P is much poorer electron conductor which still results in the continuous growth of the interphase layer, though to a lesser extent than in the $Na_{2.25}Y_{0.25}Zr_{0.75}Cl_6$ system.

$Na_4(B_{10}H_{10})(B_{12}H_{12})$ was found to not form any detectable interphase products throughout the experimental conditions tested in this study. This indicates that this borohydride material is highly electrochemically stable against the anode and is therefore a suitable candidate for the design of an anode-free sodium all-solid-state battery. When this material was evaluated a significant increase in cell efficiency was observed (4% to 64%). Since the first of the four criteria was achieved, attention shifted to the second. Aluminum foil was found to form inhomogeneous contact with the solid electrolyte layer resulting in non-uniform sodium plating and stripping. This problem was solved using a novel approach in which micron sized aluminum power was spread over the surface of the solid electrolyte separator. The liquid-like flow of the powder enabled the current collector to form intimate solid-solid contact with the solid electrolyte when pressed under 370 MPa. This resulted in the second criteria being met.

$Na_4(B_{10}H_{10})(B_{12}H_{12})$ was found to become almost completely dense after pressing at 370 MPa during battery fabrication. Due to the naturally soft nature of this material the third criteria was met. Similarly, aluminum is the softest current collector material that does not react with sodium. This works to the advantage of these cells, as the aluminum current collector was also found to be almost completely dense after pressing, thus achieving the fourth and final criteria. In this cell configuration, capacities as high as 7 mAh/cm^2 and current densities > 10 mA/cm^2 can be cycled. Furthermore, in a full-cell configuration, the battery can be cycled hundreds of times while retaining most of its capacity.

Although an anode-free cell was successfully cycled, there are still several other limitations still facing this type of battery. First are material considerations. Specifically, more work is needed on the cathode side of the battery. The $NaCrO_2$ cathode used in this study is very stable, however its voltage and capacity are low which limits the cell energy density. Other cathodes like Na_2S should be explored to solve this limitation as sulfur can store much more sodium than most layered oxide materials. Additionally, sulfur is the ideal cathode material due to its extremely low cost compared to transition metals.

The catholyte also limits the performance of the cathode composite. Currently, chloride materials are used due to their high oxidative stability. However, they typically have relatively low ionic conductivities which significantly limits the rate performance of the battery. Other novel catholyte materials should be developed to increase the ionic conductivity. Some promising candidates seem to be oxychlorides and carborates however there is little knowledge of these materials outside of their lithium counterparts.

Besides material considerations, there are many engineering challenges that stand in the way of commercialization. The biggest hurdle is the stack pressure required by most solid-state batteries during operation. Pressures around tens to hundreds of MPa are difficult to achieve in a low cost and lightweight battery casing. Therefore, the stack pressure used for cycling these batteries should be lowered to ideally < 1 MPa. Although this introduces cyclability challenges due to the natural difficulty in maintaining intimate solid-solid contact between the components of the battery, an anode-free or sodium metal anode is one path to reducing the pressure requirement. Additionally, increasing temperature is another tuning knob for enabling lower pressure cycling (< 1 MPa) as shown in this work however it is not ideal since it requires additional energy and cost

to keep a battery hot. Other strategies should be explored to optimize cell performance under lower pressures.

As all cells shown in this work are pellets comprised of compacted powdered materials, it is expected that challenges will arise when attempting to make these cells in a larger commercial format. Although this current work proposes a scalable manufacturing method for the aluminum current collector, the other components of the cell have yet to receive such attention. This includes creating a thin (10 μm) solid electrolyte separator layer and a thick (5 mAh/cm^2) cathode layer. Techniques such as slurry casting and dry processing have been used previously for lithium solid-state batteries, however, there have been few reports addressing these issues in sodium-based systems. The varying mechanical properties of sodium materials compared to their lithium counterparts will likely play a large role in the optimization of these processes and the established methods for lithium materials can likely not be relied upon.

SUPPLEMENTARY FIGURES

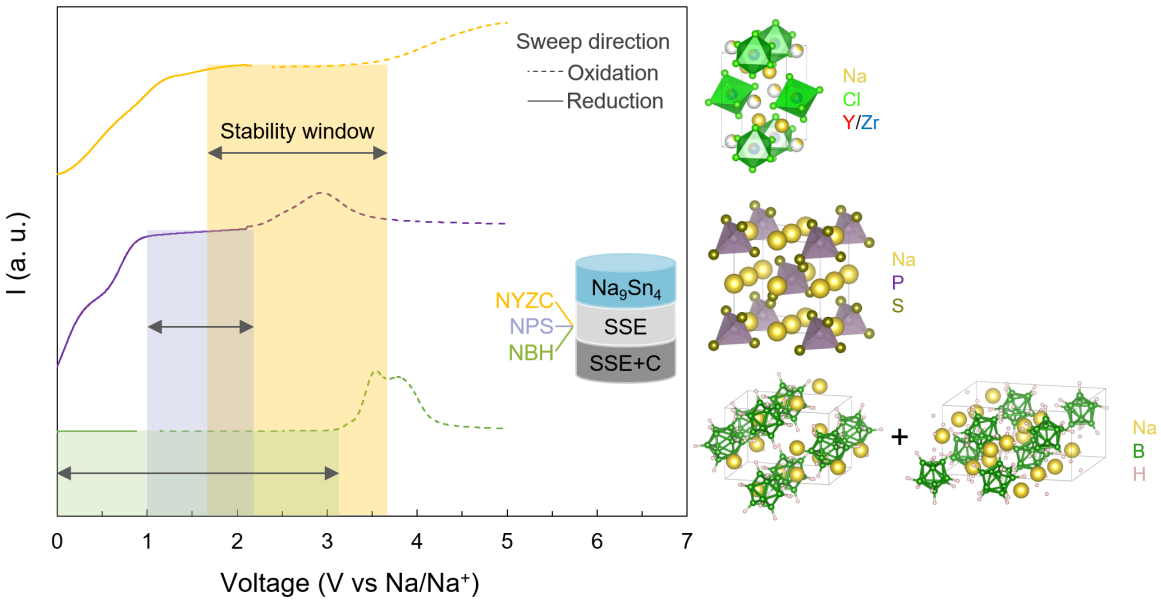

Supplementary Figure 1. Linear sweep voltammograms for NYZC, NPS, and NBH.

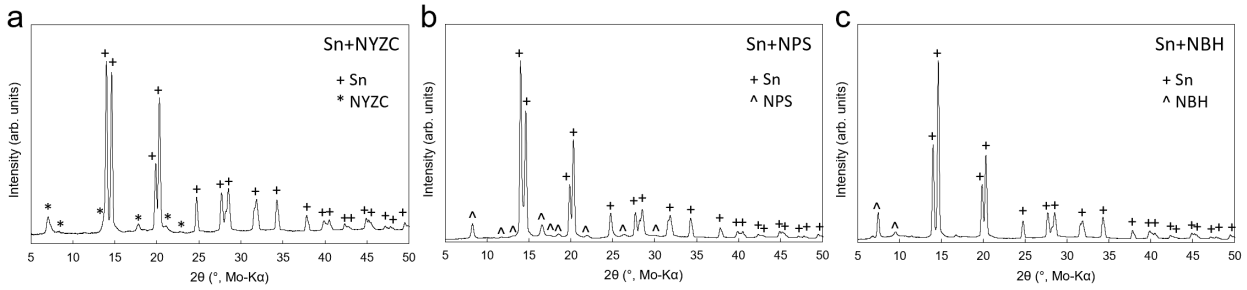

Supplementary Figure 2. XRD patterns for mixtures of Sn with a) NYZC, b) NPS, and c) NBH after heating at 80 °C for 10 h.

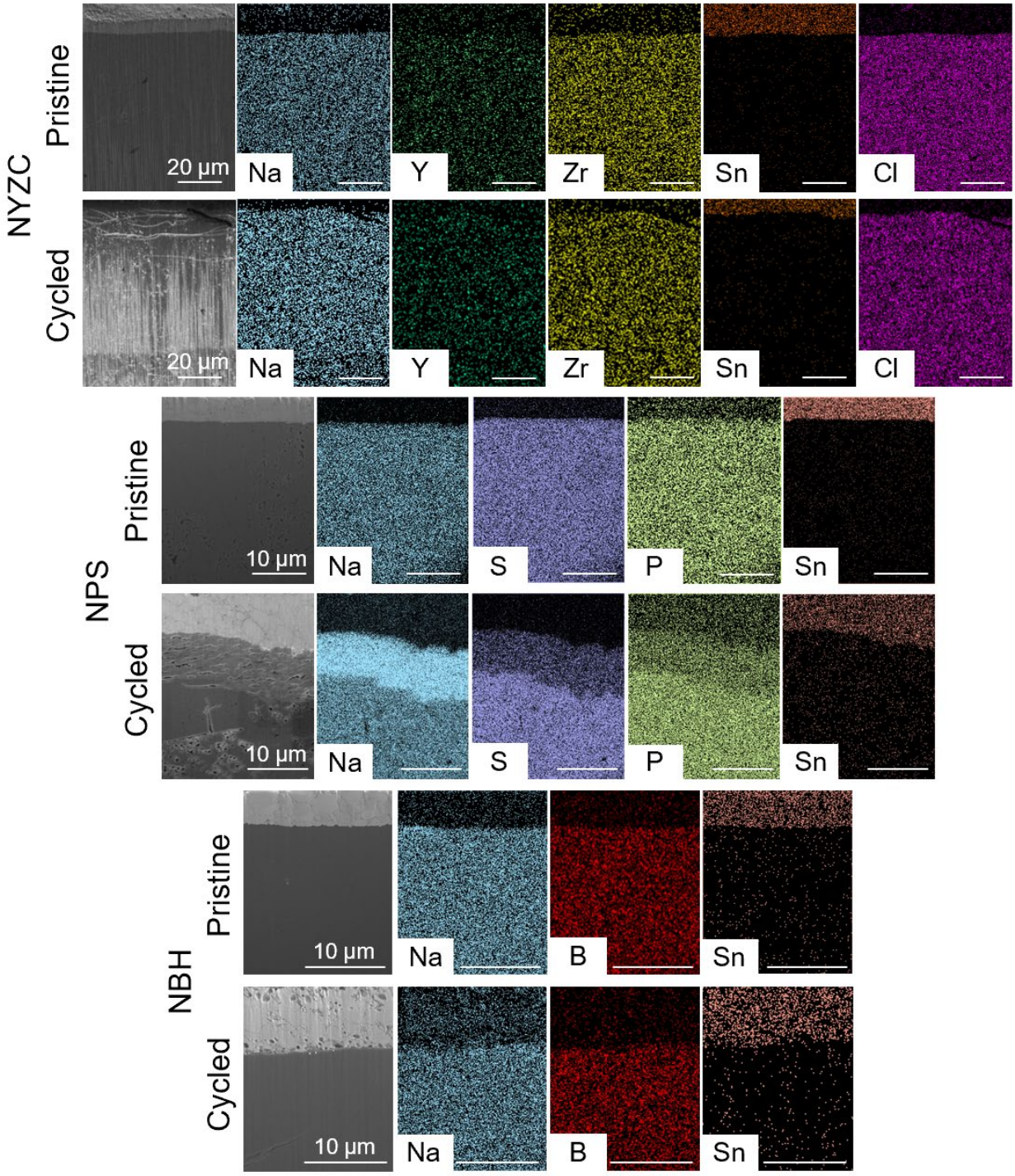

Supplementary Figure 3. FIB-SEM with EDS mapping of Sn | SSE | Na_9Sn_4 cells.

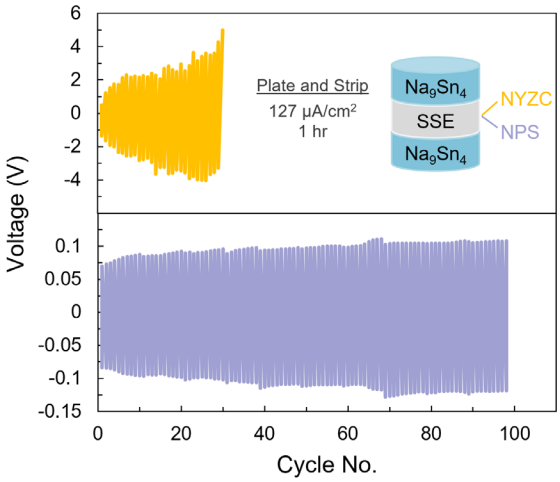

Supplementary Figure 4. Symmetric cell evaluation using NYZC and NPS electrolytes.

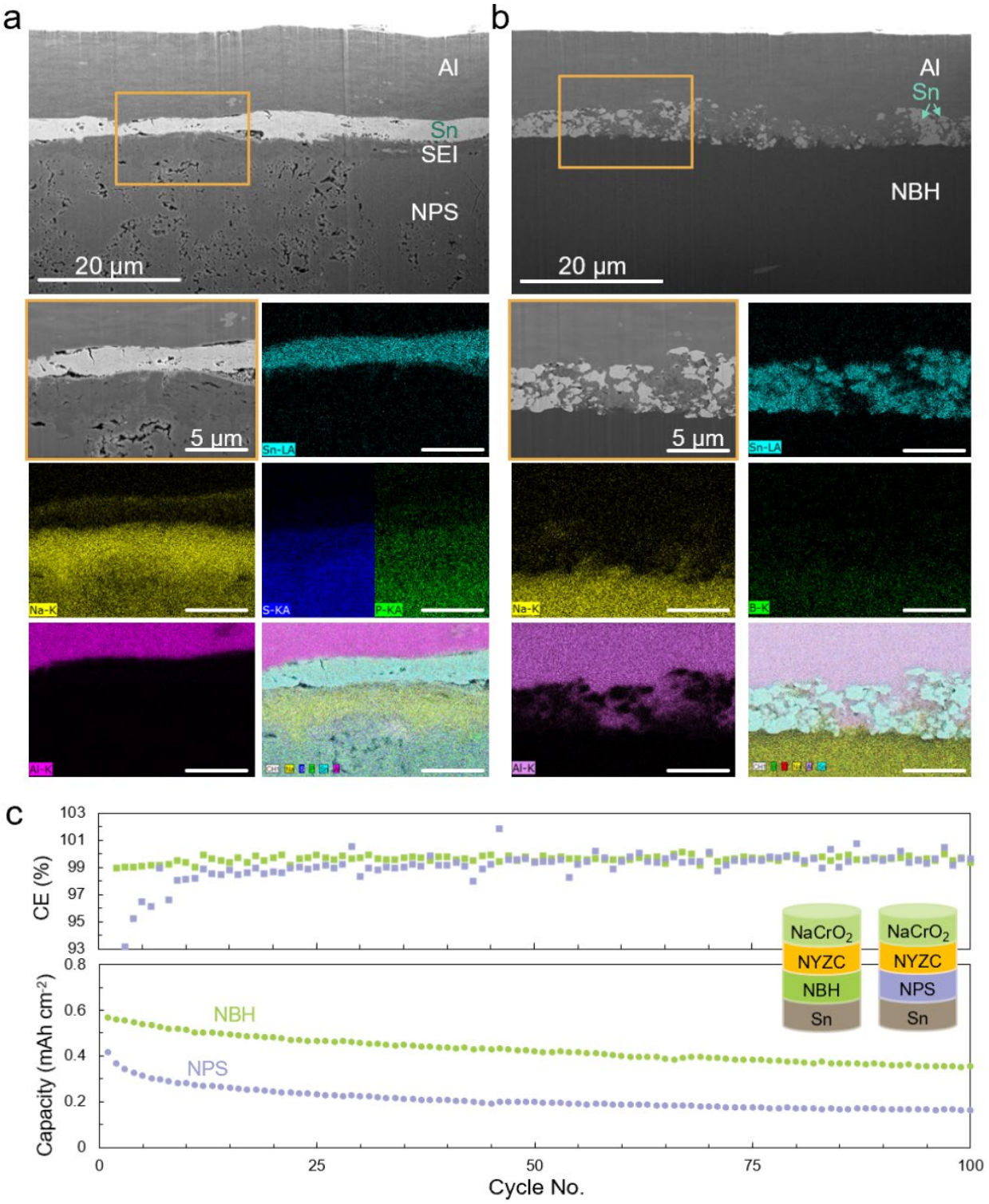

Supplementary Figure 5. FIB-SEM anode cross-section and EDS elemental mapping for (a) Sn | NPS | NYZC | $NaCrO_2$ and (b) Sn | NBH | NYZC | $NaCrO_2$ cells after cycling. (c) Electrochemical cycling data for both cells.

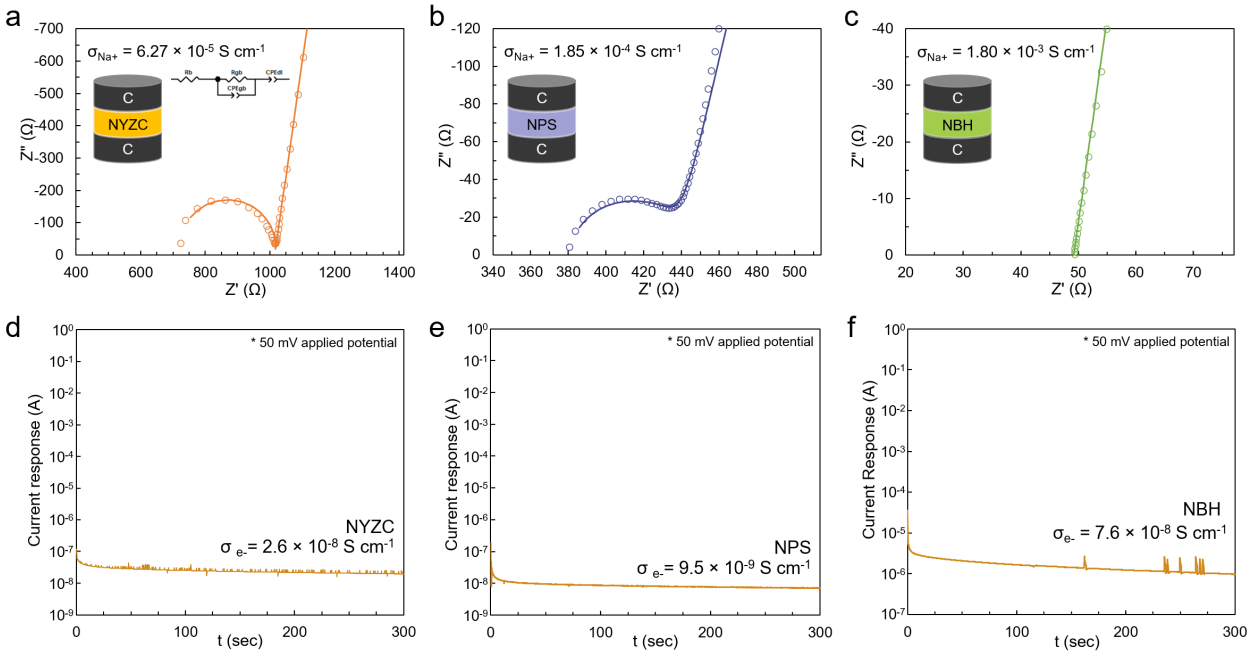

Supplementary Figure 6. EIS measurements of (a) NYZC, (b) NPS, and (c) NBH showing Na^+ conductivities of 0.0627, 0.185, and 1.8 mS/cm respectively. DC Polarization measurements of (d) NYZC, (e) NPS, and (f) NBH showing e^- conductivities of 26, 10, and 76 nS/cm respectively.

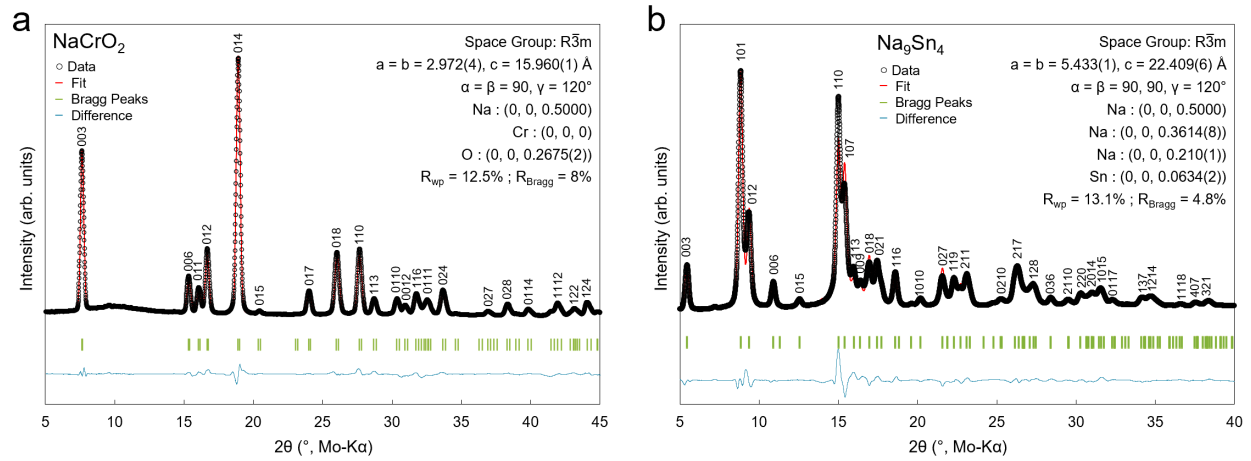

Supplementary Figure 7. XRD refinement results of (a) $NaCrO_2$ and (b) Na_9Sn_4.

Supplementary Table 1. Values used for energy density calculations.

Cathode Assumptions	
Areal Capacity	5 mAh/cm^2
$NaCrO_2$	
Nominal Voltage (vs Na/Na$^+$)	3 V
Capacity	120 mAh/g
Density	4.36 g/cm^3
$Na_3V_2(PO_4)_3$	
Nominal Voltage (vs Na/Na$^+$)	3.4 V
Capacity	118 mAh/g
Density	3.21 g/cm^3
$Na_4MnCr(PO_4)_3$	
Nominal Voltage (vs Na/Na$^+$)	3.53 V
Capacity	161 mAh/g
Density	3.26 g/cm^3
Composite Information	
Active Material wt. %	85%
a-NYZC wt. %	14%
VGCF wt. %	1%
a-NYZC Density	1.15 g/cm^3
VGCF Density	1.9 g/cm^3

Anode Assumptions	
Anode-Free	
Nominal Voltage (vs Na/Na$^+$)	0.00 V
Specific Capacity	∞ mAh/g
Density	0 g/cm^3
Sn	
Nominal Voltage (vs Na/Na$^+$)	0.26 V
Specific Capacity	847 mAh/g
Density	6.96 g/cm^3
Sb	
Nominal Voltage (vs Na/Na$^+$)	0.51 V
Specific Capacity	660 mAh/g
Density	6.29 g/cm^3
Bi	
Nominal Voltage (vs Na/Na$^+$)	0.57 V
Specific Capacity	385 mAh/g
Density	9.45 g/cm^3
Hard Carbon	
Nominal Voltage (vs Na/Na$^+$)	0.34 V
Specific Capacity	250 mAh/g
Density	1.5 g/cm^3

Electrolyte Assumptions	
Catholyte	*a*-NYZC
Anolyte	NBH
NBH Density	1.12 g/cm^3
Bi-layer Separator	
a-NYZC thickness	5 µm
NBH thickness	10 µm

Current Collector Assumptions	
Cathode CC	Al
Anode CC	Al
Cathode CC thickness	15 µm
Anode CC thickness	15 µm
Al Density	2.7 g/cm^3

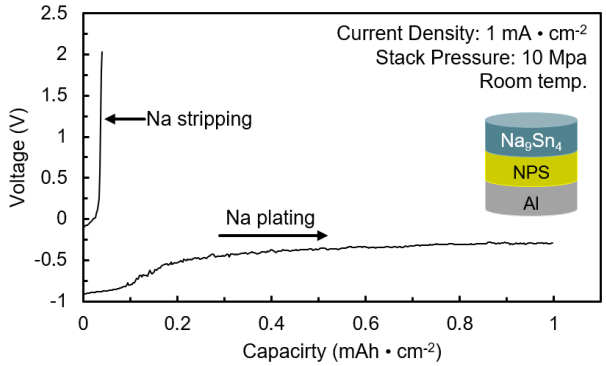

Supplementary Figure 8. Voltage curve for an anode-free half-cell using Na_3PS_4 solid electrolyte. 1 mA•cm^{-2} current density, 10 MPa stack pressure, and room temperature conditions were used for this electrochemical cycling.

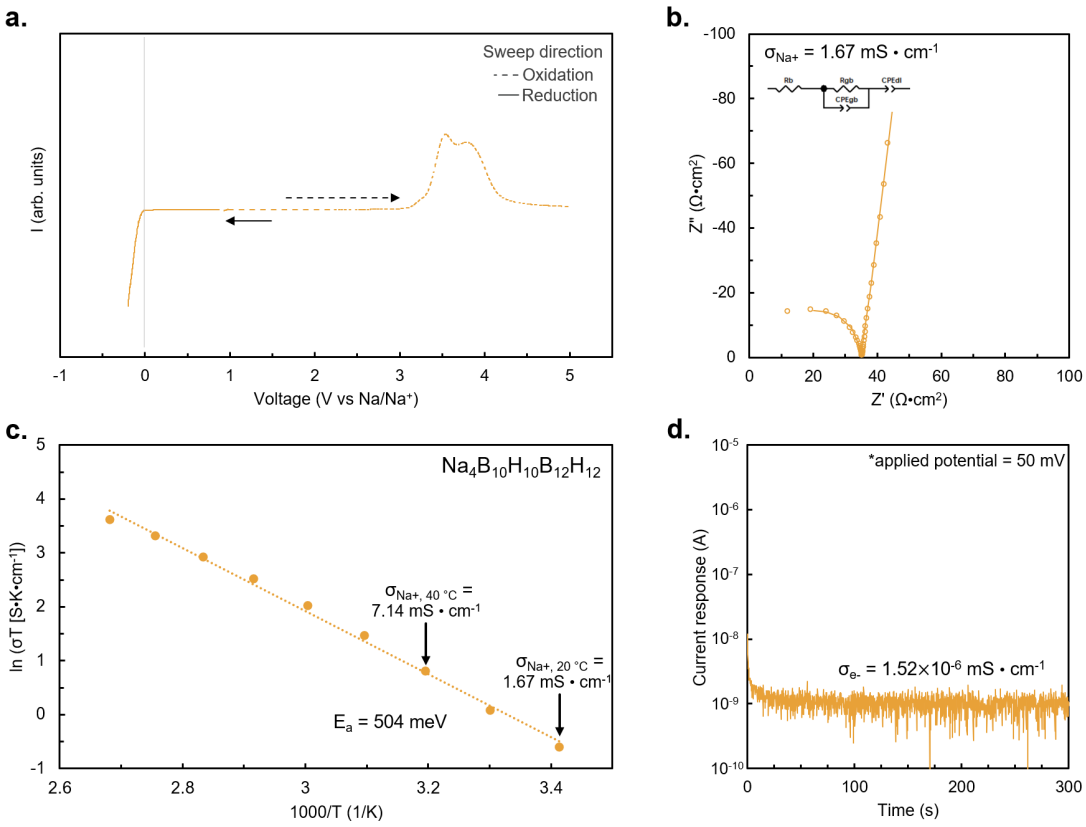

Supplementary Figure 9. NBH analysis. $Na_4(B_{10}H_{10})(B_{12}H_{12})$ a) LSV electrochemical stability window, b) EIS ionic conductivity, c) Arrhenius measurement showing the ionic conductivity as a function of temperature, and d) DC polarization electronic conductivity measurements.

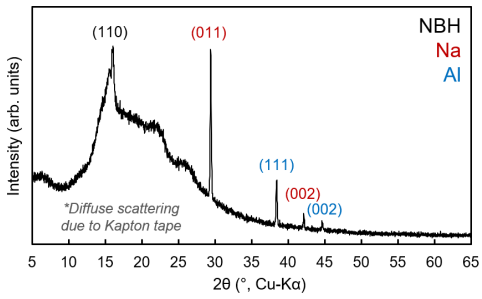

Supplementary Figure 10. XRD pattern showing the presence of metallic sodium on the surface of an Al current collector.

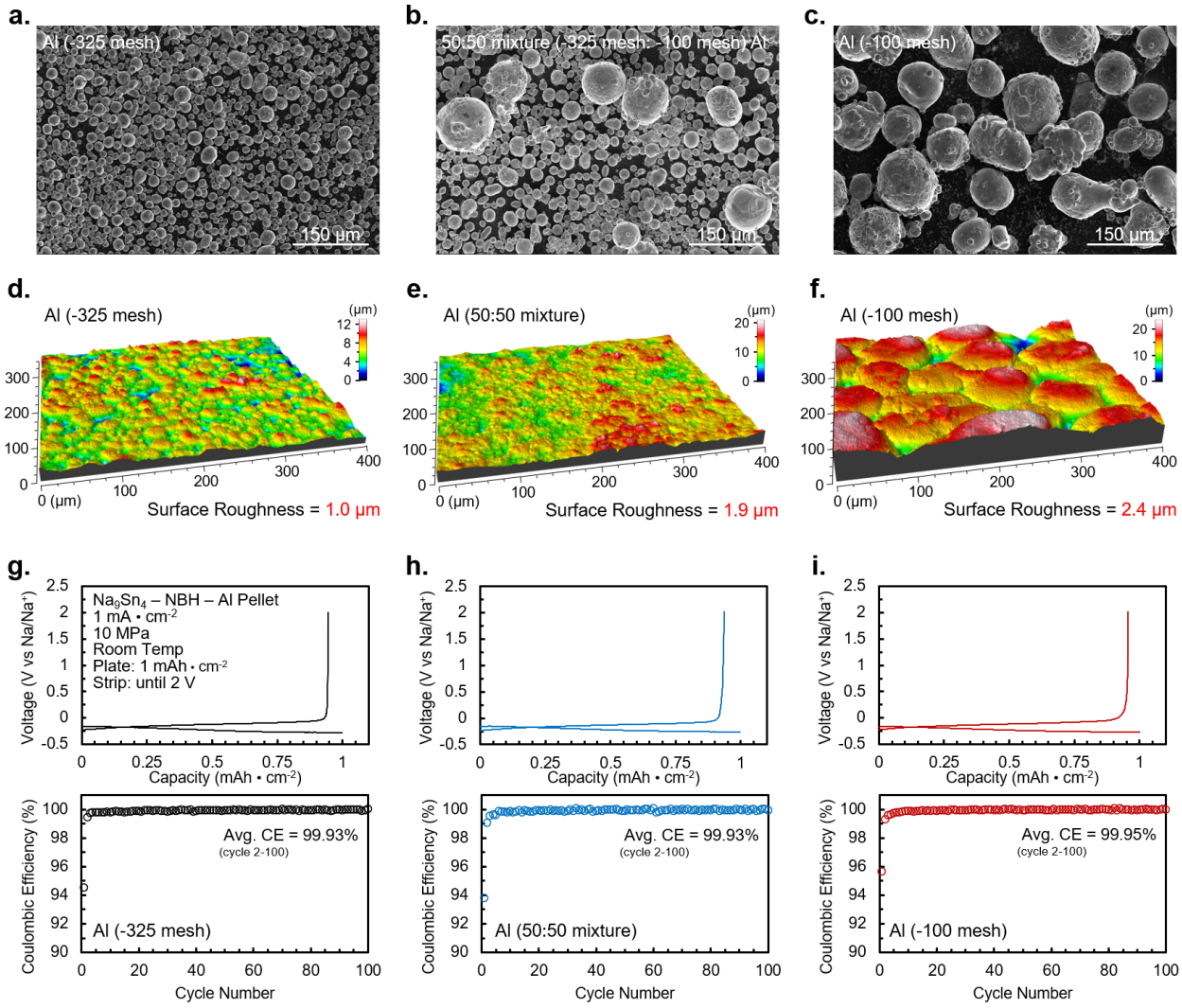

Supplementary Figure 11. Comparison of various Al particle sizes used for Al pellet fabrication. SEM of a) -325 mesh Al, b) a 50:50 wt. mixture of -325 mesh and -100 mesh Al, and c) -100 mesh Al particles. d-e) Optical profilometry of Al pellets fabricated with these Al particles. g-i) Electrochemical performance of anode-free half-cells using these three Al pellet current collectors. 1 mA•cm^{-2} current density, 10 MPa stack pressure, and room temperature conditions were used for this electrochemical cycling.

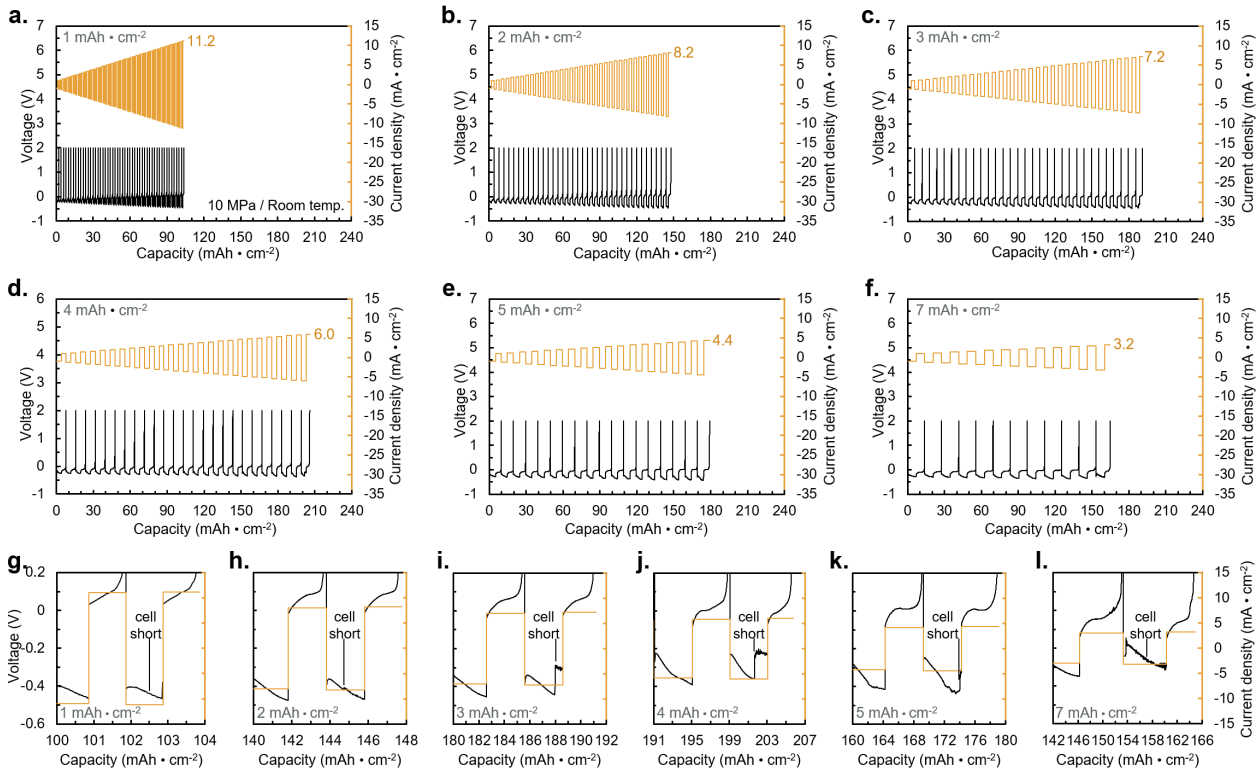

Supplementary Figure 12. Full critical current density data of anode-free (sodium). Plating/stripping data for the current ramp test used to evaluate the critical current density at a) 1, b) 2, c) 3, d) 4, e) 5 and f) 7 mAh cm^{-2} plating/stripping capacities at room temperature. Zoom-in views of the cell short observed for the same g) 1, h) 2, i) 3, j) 4, k) 5 and l) 7 mAh cm^{-2} cells. 10 MPa stack pressure at room temperature was used for this cycling data.

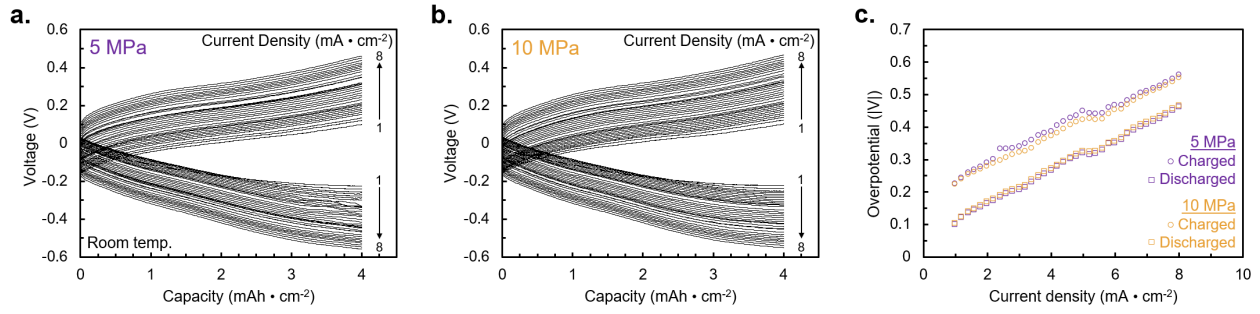

Supplementary Figure 13. High current density testing of Na_9Sn_4. Current density ramp tests at room temperature for Na_9Sn_4 | NBH | Na_9Sn_4 symmetric cells with stack pressures of a) 5 and b) 10 MPa with a current step size of 0.2 mA•cm^{-2}. A charge transfer of 4 mAh•cm^{-2} was used for all cells. c) Potential as a function of current after 4 mAh•cm^{-2} capacity transferred for both cells. Both cells were cycled at room temperature.

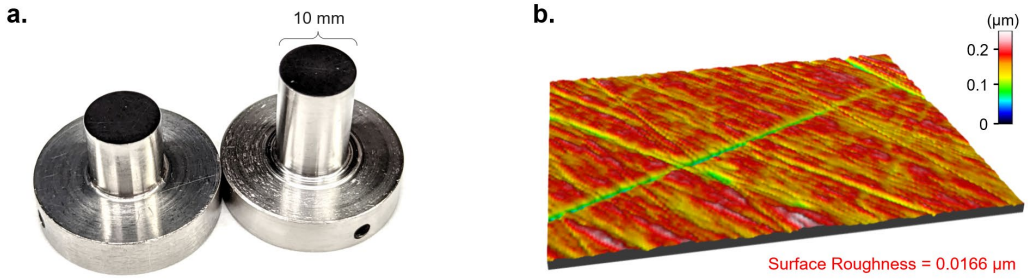

Supplementary Figure 14. Ti plunger surface characterization. a) Optical image of the plunger surface. b) Optical profilometry map showing the surface topography of the plunger surface.

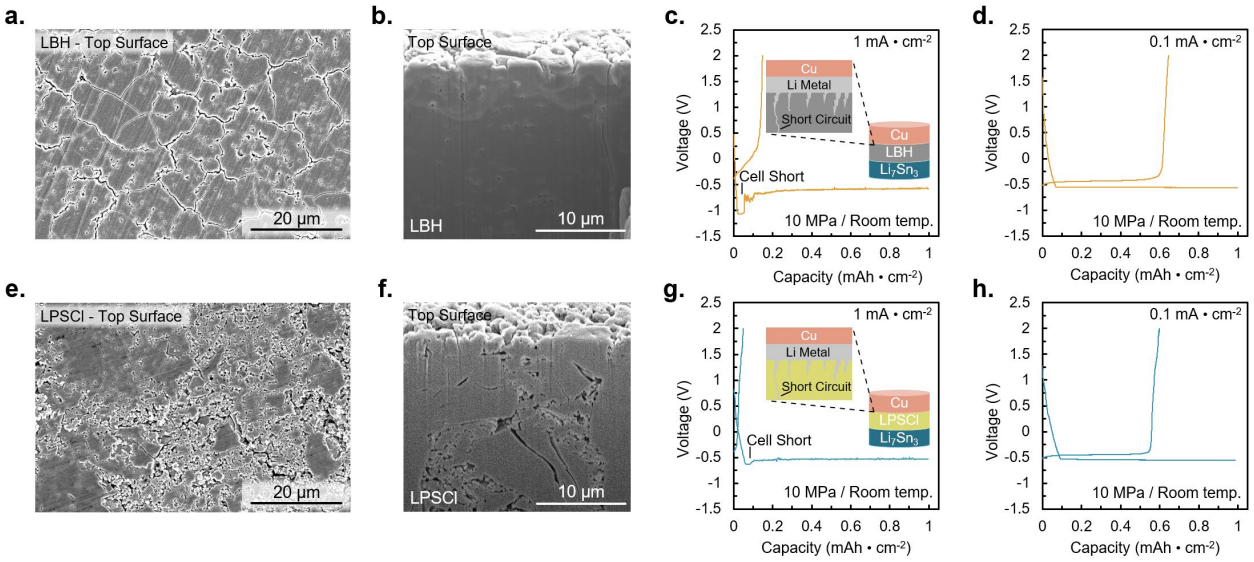

Supplementary Figure 15. Comparison of lithium-based anode-free batteries. SEM of LBH separator a) top surface and b) cross section. Cycling data of a Li_7Sn_3-LBH-Cu half-cell at c) 1 mA cm^{-2} and d) 0.1 mA cm^{-2}. SEM of LPSCl separator e) top surface and f) cross section. Cycling data of a Li_7Sn_3-LPSCl-Cu half-cell at g) 1 mA cm^{-2} and h) 0.1 mA cm^{-2}. All cells were cycled under 10 MPa stack pressure at room temperature.

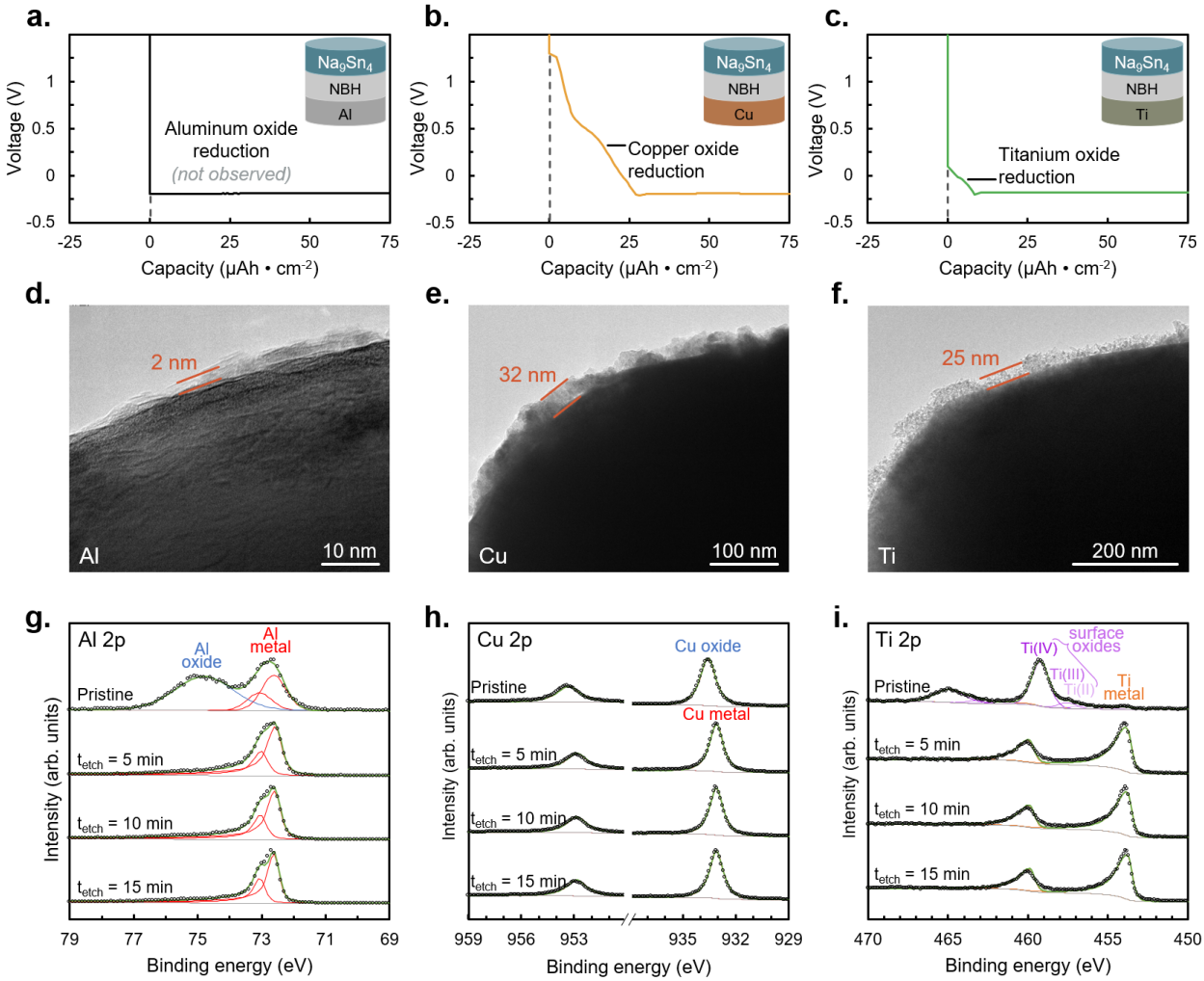

Supplementary Figure 16. Current collector surface oxide analysis. Voltage profiles of anode-free half cells using a) Al, b) Cu, and c) Ti current collectors. TEM of d) Al, e) Cu, and f) Ti particles showing the thicknesses of surface oxide layers. XPS spectra during depth profiling showing the presence of metal-oxides only on the surface of g) Al, h) Cu, and i) Ti.

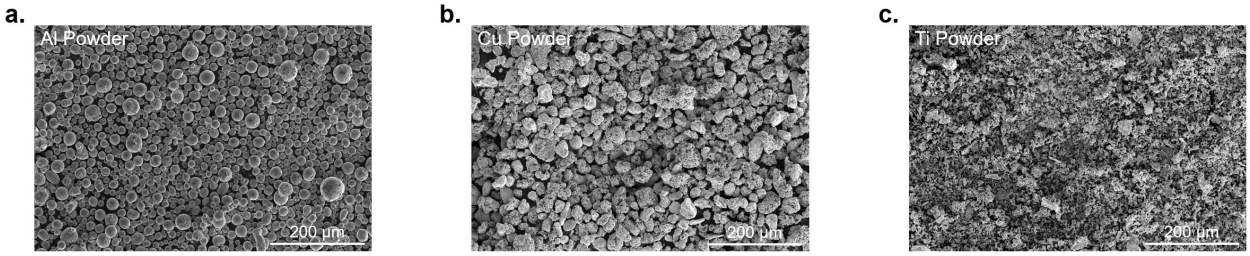

Supplementary Figure 17. Particle morphology evaluated by SEM for a) Al, b) Cu, and c) Ti powders.

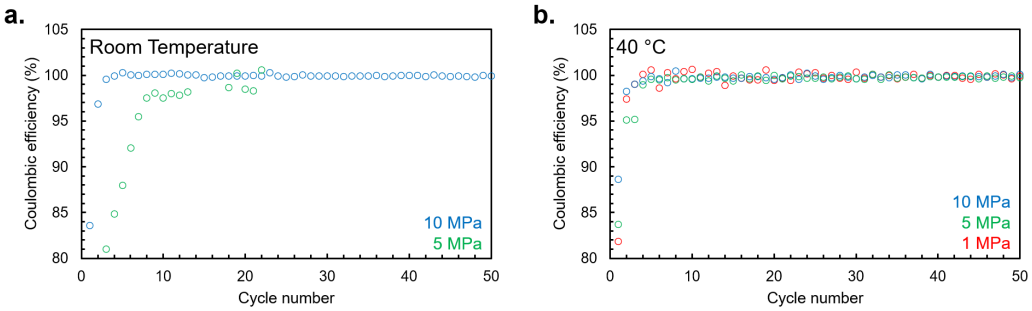

Supplementary Figure 18. Low pressure cycling. Low pressure cycling efficiency for half-cells at a) room temperature and b) 40 °C. 1 mAh • cm^{-2} plating capacity was used every cycle followed by a stripping step until a 2 V cutoff. 1 mA • cm^{-2} current density was used.

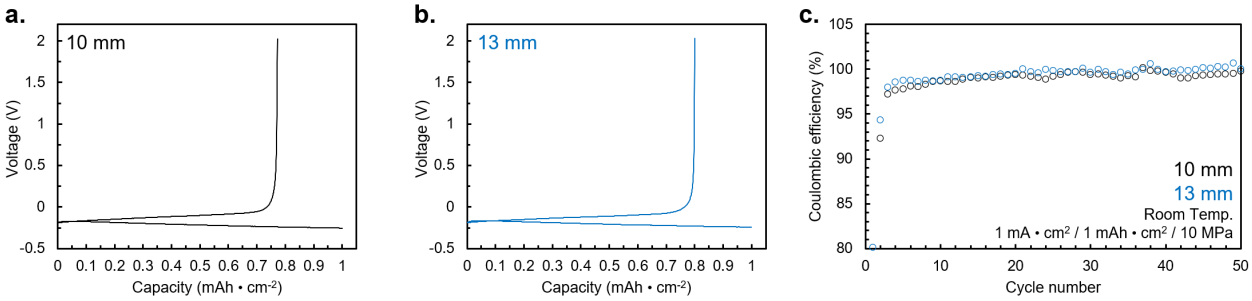

Supplementary Figure 19. Larger area cycling. Cycling efficiency for a) 10 mm and b) 13 mm diameter half-cells. 1 mAh • cm^{-2} plating capacity was used every cycle followed by a stripping step until a 2 V cutoff. Both cells were cycled under 10 MPa stack pressure at room temperature.

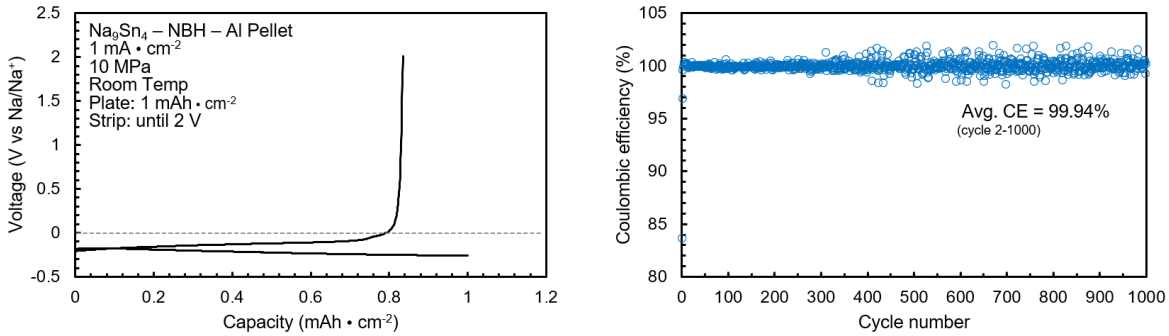

Supplementary Figure 20. Long cycling data for an anode-free half-cell.

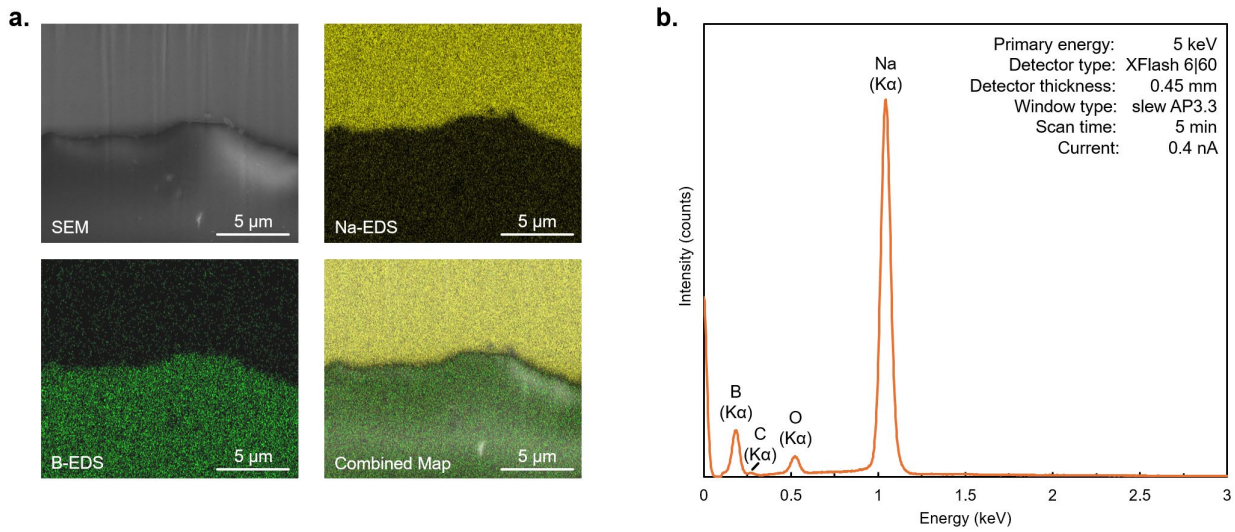

Supplementary Figure 21. EDS elemental mapping of the interface between plated Na metal and NBH solid electrolyte. b) Raw spectrum data for the sample.

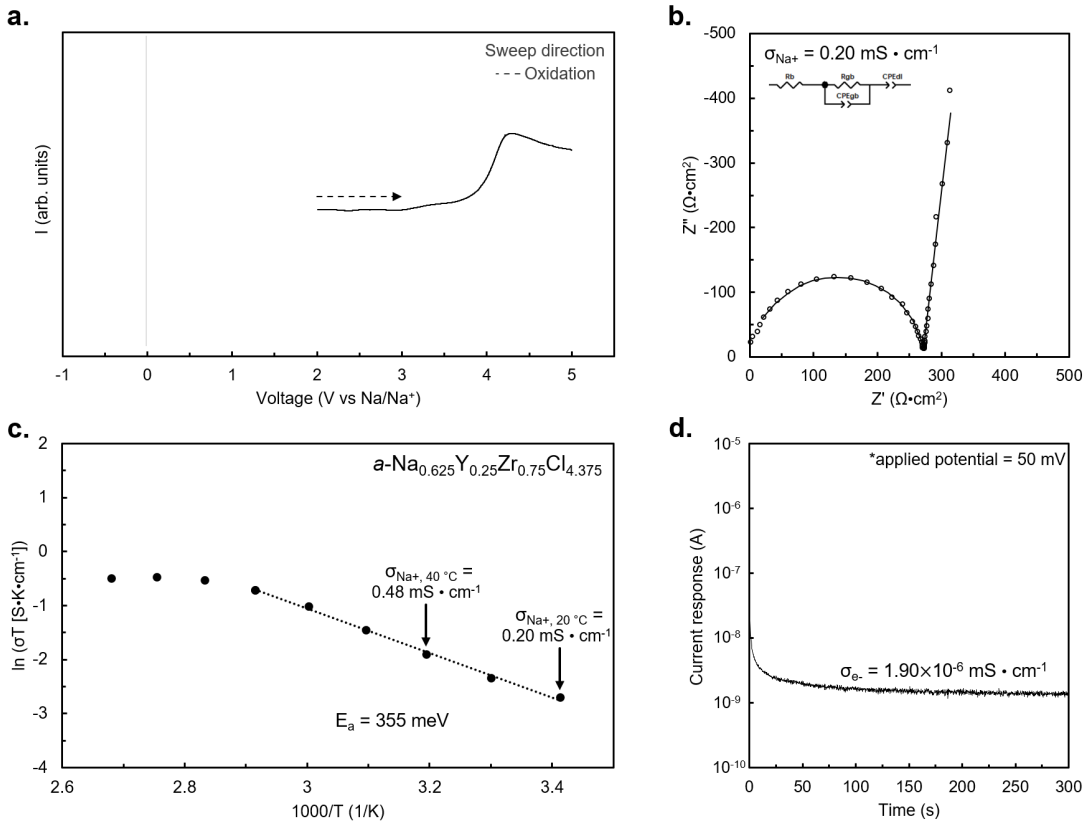

Supplementary Figure 22. Catholyte analysis. *a*-$Na_{0.625}Y_{0.25}Zr_{0.75}Cl_{4.375}$ a) LSV electrochemical stability window, b) EIS ionic conductivity, c) Arrhenius measurement showing the ionic conductivity as a function of temperature, and d) DC polarization electronic conductivity measurements.

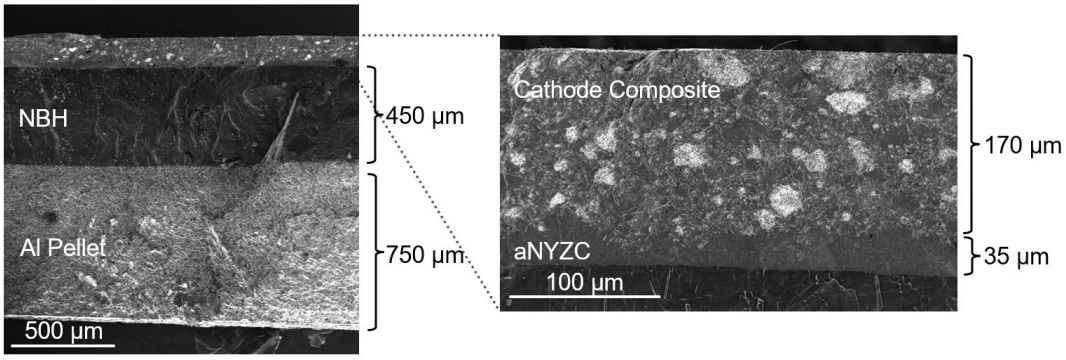

Supplementary Figure 23. SEM cross section of the anode-free cell showing the thickness of each layer.

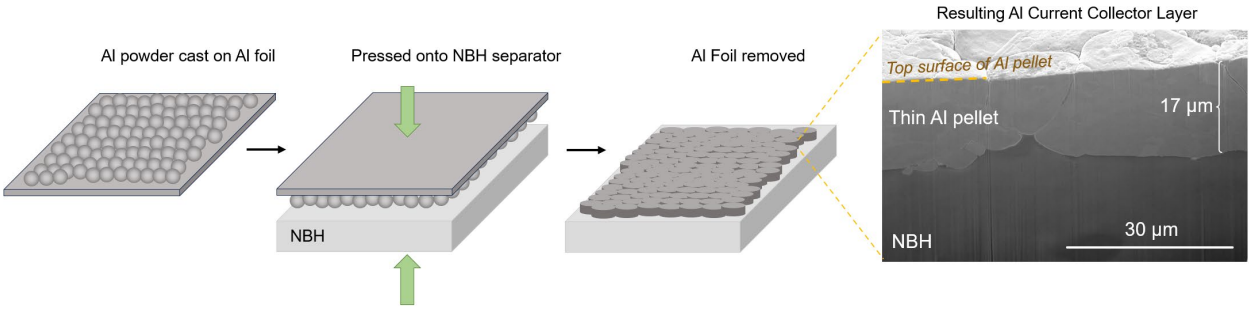

Supplementary Figure 24. Transfer process for enabling thin aluminum pellet current collectors for achieving higher energy density.

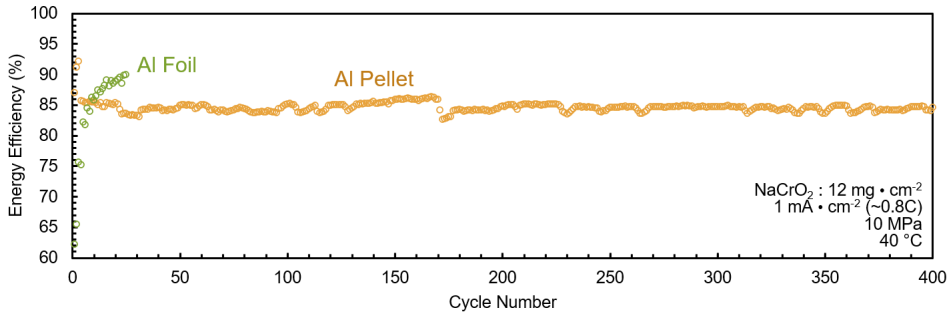

Supplementary Figure 25. Energy efficiency of the $NaCrO_2$-aNYZC-NBH-Al full cells shown in Fig. 7.

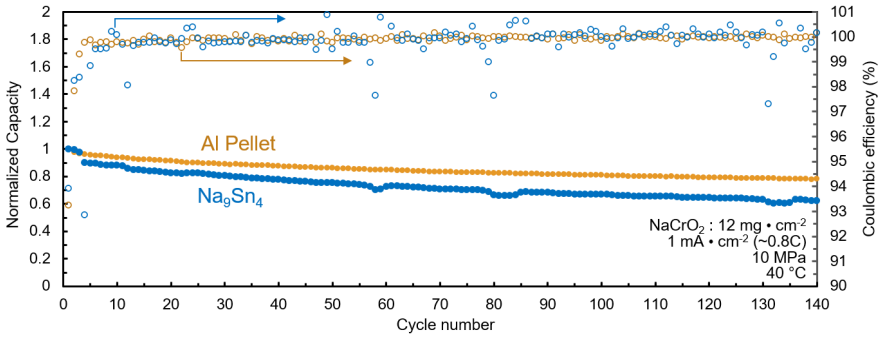

Supplementary Figure 26. Comparison between an $NaCrO_2$ composite-aNYZC-NBH-Al Pellet cell and a cell using Na_9Sn_4 as the anode material.

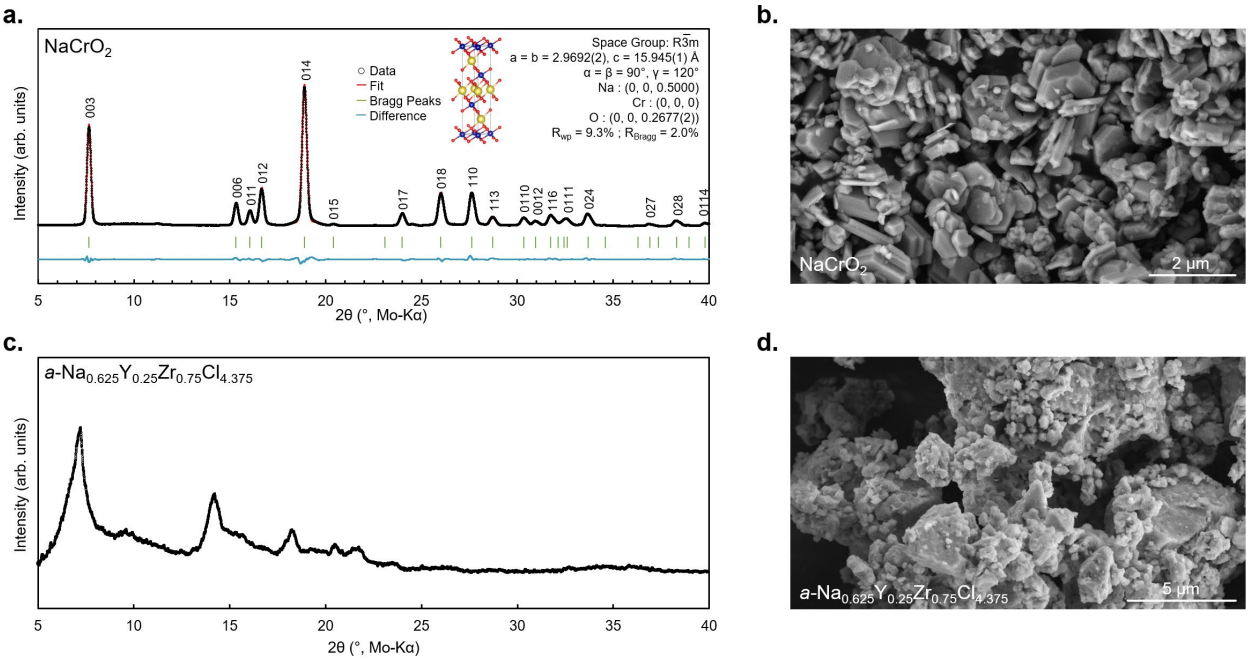

Supplementary Figure 27. Cathode and catholyte analysis. $NaCrO_2$ a) XRD refinement and b) SEM. *a*-$Na_{0.625}Y_{0.25}Zr_{0.75}Cl_{4.375}$ c) XRD and d) SEM.

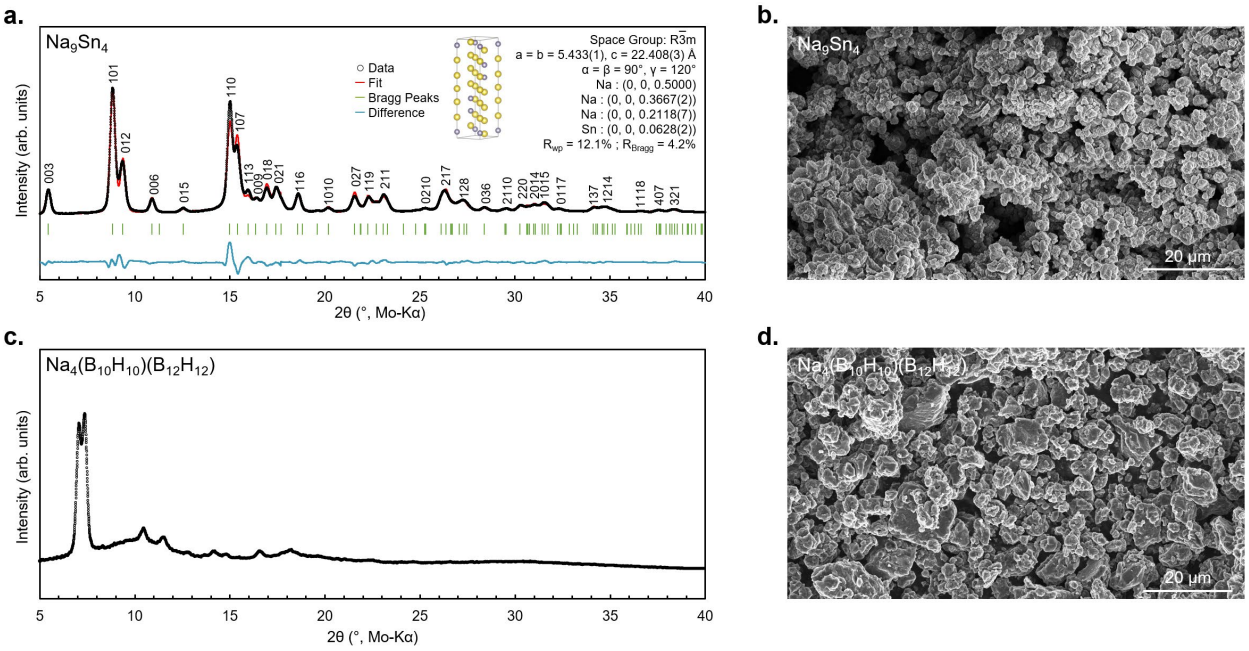

Supplementary Figure 28. NBH and counter electrode analysis. Na_9Sn_4 a) XRD refinement and b) SEM. $Na_4(B_{10}H_{10})(B_{12}H_{12})$ c) XRD and d) SEM.

REFERENCES

1. Nishi, Y. The Dawn of Lithium-Ion Batteries. *Electrochem. Soc. Interface* **25**, 71 (2016).

2. Hirsh, H. S., Li, Y., Tan, D. H. S., Zhang, M., Zhao, E. & Meng, Y. S. Sodium-Ion Batteries Paving the Way for Grid Energy Storage. *Advanced Energy Materials* **10**, 2001274 (2020).

3. Qian, J., Adams, B. D., Zheng, J., Xu, W., Henderson, W. A., Wang, J., Bowden, M. E., Xu, S., Hu, J. & Zhang, J-G. Anode-Free Rechargeable Lithium Metal Batteries. *Advanced Functional Materials* **26**, 7094–7102 (2016).

4. Fang, C., Li, J., Zhang, M., Zhang, Y., Yang, F., Lee, J. Z., Lee, M-H., Alvarado, J., Xhroeder, M. A., Yang, Y., Lu, B., Williams, N., Ceja, M., Yang, L., Cai, M., Gu, J., Xu, K., Wang, X. & Meng, Y. S. Quantifying inactive lithium in lithium metal batteries. *Nature* **572**, 511–515 (2019).

5. Tang, S., Qiu, Z., Wang, X. Y., Gu, Y., Zhang, X. G., Wang, W. W., Yan, J. W., Zheng, M. S., Dong, Q. F. & Mao, B. W. A room-temperature sodium metal anode enabled by a sodiophilic layer. *Nano Energy* **48**, 101–106 (2018).

6. Wu, H., Jia, H., Wang, C., Zhang, J.-G. & Xu, W. Recent Progress in Understanding Solid Electrolyte Interphase on Lithium Metal Anodes. *Advanced Energy Materials* **11**, 2003092 (2021).

7. Matios, E., Wang, H., Wang, C. & Li, W. Enabling Safe Sodium Metal Batteries by Solid Electrolyte Interphase Engineering: A Review. *Ind. Eng. Chem. Res.* **58**, 9758–9780 (2019).

8. Zhang, Z., Li, Y., Xu, R., Zhou, W., Li, Y., Oyakhire, S. T., Wu, Y., Xu, J., Wang, H., Yu, Z. & Boyle, D. T. Capturing the swelling of solid-electrolyte interphase in lithium metal batteries. *Science* **375**, 66–70 (2022).

9. Gao, L., Chen, J., Chen, Q. & Kong, X. The chemical evolution of solid electrolyte interface in sodium metal batteries. *Science Advances* **8**, eabm4606 (2022).

10. Wang, Y., Wang, Y., Wang, Y. X., Feng, X., Chen, W., Ai, X., Yang, H. & Cao, Y. Developments and Perspectives on Emerging High-Energy-Density Sodium-Metal Batteries. *Chem* **5**, 2547–2570 (2019).

11. Lu, Z., Yang, H., Yang, Q.-H., He, P. & Zhou, H. Building a Beyond Concentrated Electrolyte for High-Voltage Anode-Free Rechargeable Sodium Batteries. *Angewandte Chemie International Edition* **61**, e202200410 (2022).

12. Mao, M., Ji, X., Wang, Q., Ling, Z., Li, M., Liu, T., Wang, C., Hu, Y. S., Li, H., Huang, X. & Chen, L.. Anion-enrichment interface enables high-voltage anode-free lithium metal batteries. *Nat Commun* **14**, 1082 (2023).

13. Su, L., Charalambous, H., Cui, Z. & Manthiram, A. High-efficiency, anode-free lithium–metal batteries with a close-packed homogeneous lithium morphology. *Energy Environ. Sci.* **15**, 843–854 (2022).

14. Lin, C.-C., Chen, Z., Euchner, H., Eisenmann, T., Geng, K., Diemant, T., Fang, S., Yen, C. H., Passerini, S., Hu, C. C. & Bresser, D. Nanotwinned Copper Foil for "Zero Excess" Lithium–Metal Batteries. *ACS Appl. Energy Mater.* **6**, 2140–2150 (2023).

15. Louli, A. J., Genovese, M., Weber, R., Hames, S. G., Logan, E. R. & Dahn, J. R. Exploring the Impact of Mechanical Pressure on the Performance of Anode-Free Lithium Metal Cells. *J. Electrochem. Soc.* **166**, A1291 (2019).

16. Shin, W. & Manthiram, A. A Facile Potential Hold Method for Fostering an Inorganic Solid-Electrolyte Interphase for Anode-Free Lithium-Metal Batteries. *Angewandte Chemie International Edition* **61**, e202115909 (2022).

17. Spencer Jolly, D., Ning, Z., Darnbrough, J. E., Kasemchainan, J., Hartley, G. O., Adamson, P., Armstrong, D. E., Marrow, J. & Bruce, P. G. Sodium/Na β″ Alumina Interface: Effect of Pressure on Voids. *ACS Appl. Mater. Interfaces* **12**, 678–685 (2020).

18. Bates, J. B., Dudney, N. J., Neudecker, B., Ueda, A. & Evans, C. D. Thin-film lithium and lithium-ion batteries. *Solid State Ionics* **135**, 33–45 (2000).

19. Neudecker, B. J., Dudney, N. J. & Bates, J. B. "Lithium-Free" Thin-Film Battery with In Situ Plated Li Anode. *J. Electrochem. Soc.* **147**, 517 (2000).

20. Wang, M. J., Carmona, E., Gupta, A., Albertus, P. & Sakamoto, J. Enabling "lithium-free" manufacturing of pure lithium metal solid-state batteries through in situ plating. *Nat Commun* **11**, 5201 (2020).

21. Gu, D., Kim, H., Lee, J.-H. & Park, S. Surface-roughened current collectors for anode-free all-solid-state batteries. *Journal of Energy Chemistry* **70**, 248–257 (2022).

22. Lee, D., Kim, J., Sun, S., Kim, J., Paik, U. & Song, T. Sacrificial cathode additives for enhanced cycle performance for liquid and all–solid–state anode–free lithium secondary batteries. *Journal of Alloys and Compounds* **950**, 169910 (2023).

23. Lewis, J. A., Sandoval, S. E., Liu, Y., Nelson, D. L., Yoon, S. G., Wang, R., Zhao, Y., Tian, M., Shevchenko, P., Martinez-Paneda, E. & McDowell, M. T. Accelerated Short Circuiting in Anode-Free Solid-State Batteries Driven by Local Lithium Depletion. *Advanced Energy Materials* **13**, 2204186 (2023).

24. Lee, Y.-G., Fujiki, S., Jung, C., Suzuki, N., Yahiro, N., Omoda, R., Ko, D. S., Shiratsuchi, T., Sugimoto, T., Ryu, S. & Ku, J. H. High-energy long-cycling all-solid-state lithium metal batteries enabled by silver–carbon composite anodes. *Nat Energy* **5**, 299–308 (2020).

25. Gu, D., Kim, H., Kim, B.-K., Lee, J.-H. & Park, S. Chlorine-rich lithium argyrodite enables stable interfacial Li plating/stripping behavior in anode-free all-solid-state batteries. *CrystEngComm* **25**, 4182–4188 (2023).

26. Ortmann, T., Fuchs, T., Eckhardt, J. K., Ding, Z., Ma, Q., Tietz, F., Kubel, C., Rohnke, M. & Janek, J. Deposition of Sodium Metal at the Copper-NaSICON Interface for Reservoir-Free Solid-State Sodium Batteries. *Advanced Energy Materials* **n/a**, 2302729.

27. Heubner, C., Maletti, S., Auer, H., Huttl, J., Voigt, K., Lohrberg, O., Nikolowski, K., Partsch, M. & Michaelis, A. From Lithium-Metal toward Anode-Free Solid-State Batteries: Current Developments, Issues, and Challenges. *Advanced Functional Materials* **31(51)**, 2106608 (2021).

28. Shen, F., Dixit, M. B., Xiao, X. & Hatzell, K. B. Effect of Pore Connectivity on Li Dendrite Propagation within LLZO Electrolytes Observed with Synchrotron X-ray Tomography. *ACS Energy Lett.* **3**, 1056–1061 (2018).

29. Kazyak, E., Garcia-Mendez, R., LePage, W. S., Sharafi, A., Davis, A. L., Sanchez, A. J., Chen, K. H., Haslam, C., Sakamoto, J. & Dasgupta, N. P. Li Penetration in Ceramic Solid Electrolytes: Operando Microscopy Analysis of Morphology, Propagation, and Reversibility. *Matter* **2**, 1025–1048 (2020).

30. Luo, S., Wang, Z., Li, X., Wang, H., Ma, W., Zhang, L., Zhu, L. & Zhang, X. Growth of lithium-indium dendrites in all-solid-state lithium-based batteries with sulfide electrolytes. *Nat Commun* **12**, 6968 (2021).

31. Yuan, C., Gao, X., Jia, Y., Zhang, W., Wu, Q. & Xu, J. Coupled crack propagation and dendrite growth in solid electrolyte of all-solid-state battery. *Nano Energy* **86**, 106057 (2021).

32. Liu, S., Tang, S., Zhang, X., Wang, A., Yang, Q. H. & Luo, J. Porous Al Current Collector for Dendrite-Free Na Metal Anodes. *Nano Lett.* **17**, 5862–5868 (2017).

33. Yun, Q., He, Y. B., Lv, W., Zhao, Y., Li, B., Kang, F. & Yang, Q. H. Chemical Dealloying Derived 3D Porous Current Collector for Li Metal Anodes. *Advanced Materials* **28**, 6932–6939 (2016).

34. Poizot, P., Laruelle, S., Grugeon, S., Dupont, L. & Tarascon, J.-M. Nano-sized transition-metal oxides as negative-electrode materials for lithium-ion batteries. *Nature* **407**, 496–499 (2000).

35. Sen, U. K., Johari, P., Basu, S., Nayak, C. & Mitra, S. An experimental and computational study to understand the lithium storage mechanism in molybdenum disulfide. *Nanoscale* **6**, 10243–10254 (2014).

36. Jang, J., Kim, Y., Chae, O.B., Yoon, T., Kim, S.M., Kim, H.S., Park, H., Ryu, J.H. & Oh, S.M. A First-Cycle Coulombic Efficiency Higher than 100 % Observed for a Li2MO3 (M=Mo or Ru) Electrode. *Angewandte Chemie International Edition* **53**, 10654–10657 (2014).

37. Wu, E. A., Banerjee, S., Tang, H., Richardson, P.M., Doux, J.M., Qi, J., Zhu, Z., Grenier, A., Li, Y., Zhao, E., Deysher, G., Sebti, E., Nguyen, H., Stephens, R., Verbist, G., Chapman, K.W., Clement, R.J. & Banerjee, A. & Meng, Y.S. & Ong, S.P. A stable cathode-solid electrolyte composite for high-voltage, long-cycle-life solid-state sodium-ion batteries. *Nat Commun* **12**, 1256 (2021).

38. Connell, J. G., Fuchs, T., Hartmann, H., Krauskopf, T., Zhu, Y., Sann, J., Garcia-Mendex, R., Sakamoto, J., Tepavcevic, S. & Janek, J. Kinetic versus Thermodynamic Stability of LLZO in Contact with Lithium Metal. *Chem. Mater.* **32**, 10207–10215 (2020).

39. Fu, Y. & Ma, C. Interplay between Li3YX6 (X = Cl or Br) solid electrolytes and the Li metal anode. *Sci. China Mater.* **64**, 1378–1385 (2021).

40. Wu, E. A., Kompella, C.S., Zhu, Z., Lee, J.Z., Lee, S.C., Chu, I.H., Nguyen, H., Ong, S.P., Banerjee, A. & Meng, Y.S. New Insights into the Interphase between the Na Metal Anode and Sulfide Solid-State Electrolytes: A Joint Experimental and Computational Study. *ACS Appl. Mater. Interfaces* **10**, 10076–10086 (2018).

41. Tang, H., Deng, Z., Lin, Z., Wang, Z., Chu, I.H., Chen, C., Zhu, Z., Zheng, C. & Ong, S.P. Probing Solid–Solid Interfacial Reactions in All-Solid-State Sodium-Ion Batteries with First-Principles Calculations. *Chem. Mater.* **30**, 163–173 (2018).

42. Wenzel, S., Leichtweiss, T., Weber, D.A., Sann, J., Seier, W.G. & Janek, J. Interfacial Reactivity Benchmarking of the Sodium Ion Conductors Na3PS4 and Sodium β-Alumina for Protected Sodium Metal Anodes and Sodium All-Solid-State Batteries. *ACS Appl. Mater. Interfaces* **8**, 28216–28224 (2016).

43. Inorganic Chemistry, 2nd Edition. https://www.pearson.com/content/one-dot-com/one-dot-com/us/en/higher-education/program.html.

44. Duchêne, L., Kuhnel, R. S., Rentsch, D., Remhof, A., Hagemann, H. & Battaglia, C. A highly stable sodium solid-state electrolyte based on a dodeca/deca-borate equimolar mixture. *Chemical Communications* **53**, 4195–4198 (2017).

45. Lu, Z. & Ciucci, F. Metal Borohydrides as Electrolytes for Solid-State Li, Na, Mg, and Ca Batteries: A First-Principles Study. *Chem. Mater.* **29**, 9308–9319 (2017).

46. Banjade, H., Fang, H. & Jena, P. Metallo-boranes: a class of unconventional superhalogens defying electron counting rules. *Nanoscale* **14**, 1767–1778 (2022).

47. Rajasekharan, T. & Seshubai, V. On the electrical conductivity of transition metals. *arXiv:1102.5654 [cond-mat]* (2011).

48. Dreyfus, R. W. & Nowick, A. S. Ionic Conductivity of Doped NaCl Crystals. *Phys. Rev.* **126**, 1367–1377 (1962).

49. Abellán, G., Neiss, C., Lloret, V., Wild, S., Chacón-Torres, J.C., Werbach, K., Fedi, F., Shiozawa, H., Görling, A., Peterlik, H. & Pichler, T., 2017. Exploring the formation of black

phosphorus intercalation compounds with alkali metals. *Angewandte Chemie International Edition*, *56*(48), pp.15267-15273.

50. Yu, X., Giorgi, G., Ushiyama, H. & Yamashita, K. First-principles study of fast Na diffusion in Na3P. *Chemical Physics Letters* **612**, 129–133 (2014).

51. Ando, T., Yubuchi, S., Sakuda, A., Hayashi, A. & Tatsumisago, M. Mechanochemical Synthesis of Na-Sb Alloy Negative Electrodes and Their Application to All-solid-state Sodium Batteries. *Electrochemistry* **87**, 289–293 (2019).

52. Shengnan, Z., Dongmei, H., Shan, R., Min, X., Shuanjin, W. & Yuezhong, M., 2020. Immobilization Strategies of Organic Electrode Materials. *Progress in Chemistry*, *32*(1), p.103.

53. Tanibata, N., Deguchi, M., Hayashi, A. & Tatsumisago, M., 2017. All-solid-state Na/S batteries with a Na3PS4 electrolyte operating at room temperature. *Chemistry of Materials*, *29*(12), pp.5232-5238.

54. Chevrier, V.L. & Ceder, G., 2011. Challenges for Na-ion negative electrodes. *Journal of The Electrochemical Society*, *158*(9), p.A1011.

55. Duchêne, L., Kuhnel, R. S., Rentsch, D., Remhof, A., Hagemann, H. & Battaglia, C. A highly stable sodium solid-state electrolyte based on a dodeca/deca-borate equimolar mixture. *Chemical Communications* **53**, 4195–4198 (2017).

56. Deysher, G., Chen, Y. T., Sayahpour, B., Lin, S. W. H., Ham, S. Y., Ridley, P., Cronk, A., Wu, E. A., Tan, D. H. S., Doux, J-M., Oh, J. A. S., Jang, J., Nguyen, L. H. B. & Meng, Y. S. Evaluating Electrolyte–Anode Interface Stability in Sodium All-Solid-State Batteries. *ACS Appl. Mater. Interfaces* **14**, 47706–47715 (2022).

57. Wang, M. J., Chang, J.-Y., Wolfenstine, J. B. & Sakamoto, J. Analysis of elastic, plastic, and creep properties of sodium metal and implications for solid-state batteries. *Materialia* **12**, 100792 (2020).

58. Schlenker, R., Stepien, D., Kock, P., Hupfer, T., Indris, S., Roling, B., Mib, V., Fuchs, A., Wilhelmi, M. & Ehrenberg, H. Understanding the Lifetime of Battery Cells Based on Solid-State Li6PS5Cl Electrolyte Paired with Lithium Metal Electrode. *ACS Appl. Mater. Interfaces* **12**, 20012–20025 (2020).

59. Yang, Z., Jin, M., Cheng, S., Ma, X., Qi, Z., Zhang, J., Yang, Y. & Guo, Y. Developing a high-voltage electrolyte based on conjuncto-hydroborates for solid-state sodium batteries. *J. Mater. Chem. A* **10**, 7186–7194 (2022).

60. Jin, M., Yang, Z., Cheng, S. & Guo, Y. Fast Sodium-Ion Conduction in a Novel Conjuncto-Hydroborate of Na4B20H18. *ACS Appl. Energy Mater.* **5**, 15578–15585 (2022).

61. Kasemchainan, J., Zekoll, S., Spencer Jolly, D., Ning, Z., Hartley, G. O., Marrow, J. & Bruce, P. G. Critical stripping current leads to dendrite formation on plating in lithium anode solid electrolyte cells. *Nat. Mater.* **18**, 1105–1111 (2019).

62. Su, Y., Ye, L., Fitzhugh, W., Wang, Y., Gil-Gonzalez, E., Kim, I. & Li, X. A more stable lithium anode by mechanical constriction for solid state batteries. *Energy Environ. Sci.* **13**, 908–916 (2020).

63. Bonnick, P., Niitani, K., Nose, M., Suto, K., Arthur, T. S. & Muldoon, J. A high performance all solid state lithium sulfur battery with lithium thiophosphate solid electrolyte. *J. Mater. Chem. A* **7**, 24173–24179 (2019).

64. Fan, X., Ji, X., Han, F., Yue, J., Chen, J., Chen, L., Deng, T., Jiang, J. & Wang, C. Fluorinated solid electrolyte interphase enables highly reversible solid-state Li metal battery. *Science Advances* **4**, eaau9245 (2018).

65. Liang, J., Li, X., Zhao, Y., Goncharova, L. V., Li, W., Adair, K. R., Banis, M. N., Hu, Y., Sham T. L., Huang, H. & Zhang, L. An Air-Stable and Dendrite-Free Li Anode for Highly Stable All-Solid-State Sulfide-Based Li Batteries. *Advanced Energy Materials* **9**, 1902125 (2019).

66. Zhang, Z., Zhang, L., Yan, X., Wang, H., Liu, Y., Yu, C., Cao, X., van Eijck, L. & Wen, B. All-in-one improvement toward Li6PS5Br-Based solid electrolytes triggered by compositional tune. *Journal of Power Sources* **410–411**, 162–170 (2019).

67. Garcia-Mendez, R., Mizuno, F., Zhang, R., Arthur, T. S. & Sakamoto, J. Effect of Processing Conditions of 75Li2S-25P2S5 Solid Electrolyte on its DC Electrochemical Behavior. *Electrochimica Acta* **237**, 144–151 (2017).

68. Zhang, Z., Zhang, L., Liu, Y., Yan, X., Xu, B. & Wang, L. M. One-step solution process toward formation of Li6PS5Cl argyrodite solid electrolyte for all-solid-state lithium-ion batteries. *Journal of Alloys and Compounds* **812**, 152103 (2020).

69. Pang, B., Wu, Z., Zhang, W., Huang, H., Gan, Y., Xia, Y., He, X., Xia, C. & Zhang, J. Ag nanoparticles incorporated interlayer enables ultrahigh critical current density for Li6PS5Cl-based all-solid-state lithium batteries. *Journal of Power Sources* **563**, 232836 (2023).

70. Wu, M., Li, M., Jin, Y., Chang, X., Zhao, X., Gu, Z., Liu, G. & Yan, X. In situ formed LiF-Li3N interface layer enables ultra-stable sulfide electrolyte-based all-solid-state lithium batteries. *Journal of Energy Chemistry* **79**, 272–278 (2023).

71. Subramanian, Y., Rajagopal, R., Kang, S. & Ryu, K.-S. Enhancement of lithium argyrodite interface stability through MoO2 substitution and its application in lithium solid state batteries. *Journal of Alloys and Compounds* **925**, 166596 (2022).

72. Zou, C., Yang, L., Zang, Z., Tao, X., Yi, L., Chen, X., Liu, X., Zhang, X. & Wang, X. LiAlO2-coated LiNi0.8Co0.1Mn0.1O2 and chlorine-rich argyrodite enabling high-performance all-solid-state lithium batteries at suitable stack pressure. *Ceramics International* **49**, 443–449 (2023).

73. Subramanian, Y., Rajagopal, R. & Ryu, K.-S. Blending a Li3N/Li3YCl6 solid electrolyte with Li6PS5Cl argyrodite structure to improve interface stability and electrochemical

performance in Lithium solid-state batteries. *Journal of Alloys and Compounds* **940**, 168867 (2023).

74. Liu, Y., Su, H., Zhong, Y., Wang, X., Xia, X., Gu, C. & Tu, J. Revealing the Impact of Cl Substitution on the Crystallization Behavior and Interfacial Stability of Superionic Lithium Argyrodites. *Advanced Functional Materials* **32**, 2207978 (2022).

75. Lewis, J. A., Lee, C., Liu, Y., Han, S. Y., Prakash, D., Klein, E. J., Lee, H. W. & McDowell, M. T. Role of Areal Capacity in Determining Short Circuiting of Sulfide-Based Solid-State Batteries. *ACS Appl. Mater. Interfaces* **14**, 4051–4060 (2022).

76. Wang, G., Lin, C., Gao, C., Dong, P., Liang, B., Shen, X. & Jiao, Q. Hydrolysis-resistant and Anti-dendritic halide composite Li3PS4-LiI solid electrolyte for all-solid-state lithium batteries. *Electrochimica Acta* **428**, 140906 (2022).

77. Zhao, B., Shi, Y., Wu, J., Xing, C., Liu, Y., Ma, W., Liu, X., Jiang, Y. & Zhang, J. Stabilizing Li7P3S11/lithium metal anode interface by in-situ bifunctional composite layer. *Chemical Engineering Journal* **429**, 132411 (2022).

78. Wu, M., Liu, G. & Yao, X. Oxygen doped argyrodite electrolyte for all-solid-state lithium batteries. *Applied Physics Letters* **121**, 203904 (2022).

79. Kim, H.-M., Subramanian, Y. & Ryu, K.-S. Improved electrochemical and air stability performance of SeS2 doped argyrodite lithium superionic conductors for all-solid-state lithium batteries. *Electrochimica Acta* **442**, 141869 (2023).

80. Ni, Y., Huang, C., Liu, H., Liang, Y. & Fan, L.-Z. A High Air-Stability and Li-Metal-Compatible Li3+2xP1−xBixS4−1.5xO1.5x Sulfide Electrolyte for All-Solid-State Li–Metal Batteries. *Advanced Functional Materials* **32**, 2205998 (2022).

81. Orsini, F., Du Pasquier, A., Beaudouin, B., Tarascon, J. M., Trentin, M., Languenhuizen, N., De Beer, E. & Notten, P. In situ Scanning Electron Microscopy (SEM) observation of interfaces within plastic lithium batteries. *Journal of Power Sources* **76**, 19–29 (1998).

82. Orsini, F., Du Pasquier, A., Beaudouin, B., Tarascon, J. M., Trentin, M, Languenhuizen, N., De Beer, E. & Notten, P. In situ SEM study of the interfaces in plastic lithium cells. *Journal of Power Sources* **81–82**, 918–921 (1999).

83. Seong, I. W., Hong, C. H., Kim, B. K. & Yoon, W. Y. The effects of current density and amount of discharge on dendrite formation in the lithium powder anode electrode. *Journal of Power Sources* **178**, 769–773 (2008).

84. Zhou, C., Grinderslev, J. B., Skov, L. N., Jorgensen, M., Li, Y., Skibsted, J., Yan, Y. & Jensen, T. R. Polymorphism, ionic conductivity and electrochemical properties of lithium closo - deca- and dodeca-borates and their composites, Li 2 B 10 H 10 –Li 2 B 12 H 12. *Journal of Materials Chemistry A* **10**, 16137–16151 (2022).

85. Barai, P., Ngo, A. T., Narayanan, B., Higa, K., Curtiss, L. A. & Srinivasan, V. The Role of Local Inhomogeneities on Dendrite Growth in LLZO-Based Solid Electrolytes. *J. Electrochem. Soc.* **167**, 100537 (2020).

86. Lu, Z. & Ciucci, F. Metal Borohydrides as Electrolytes for Solid-State Li, Na, Mg, and Ca Batteries: A First-Principles Study. *Chem. Mater.* **29**, 9308–9319 (2017).

87. Murray, J. L. The Al−Na (Aluminum-Sodium) system. *Bulletin of Alloy Phase Diagrams* **4**, 407–410 (1983).

88. Pelton, A. D. The Cu−Na (Copper-Sodium) system. *Bulletin of Alloy Phase Diagrams* **7**, 25–27 (1986).

89. Bale, C. W. The Na-Ti (Sodium-Titanium) system. *Bulletin of Alloy Phase Diagrams* **10**, 138–139 (1989).

90. Samsonov, G. V. *Handbook of the Physicochemical Properties of the Elements*. (Springer Science & Business Media, 2012).

91. Tan, D. H. S., Chen, Y. T., Yang, H., Bao, W., Sreenarayanan, B., Doux, J-M., Li, W., Lu, B., Ham, S. Y., Sayahpour, B., Scharf, J., Wu, E. A., Deysher, G., Han, H. E., Hah, H. J., Jeong, H., Lee, J. B., Chen, Z. & Meng, Y. S. Carbon-free high-loading silicon anodes enabled by sulfide solid electrolytes. *Science* **373**, 1494–1499 (2021).

92. Randau, S., Weber, D. A., Kotz, O., Koerver, R., Braun, P., Weber, A., Ivers-Tiffee, E., Adermann, T., Kulisch, J., Seier, W. G. & Richter, F. H. Benchmarking the performance of all-solid-state lithium batteries. *Nat Energy* **5**, 259–270 (2020).

93. Zhou, L., Zuo, T. T., Kwok, C. Y., Kim, S. Y., Assoud, A., Zhang, Q., Janek, J. & Nazar, L. F. High areal capacity, long cycle life 4 V ceramic all-solid-state Li-ion batteries enabled by chloride solid electrolytes. *Nat Energy* **7**, 83–93 (2022).

94. Zhou, L., Kwok, C. Y., Shyamsunder, A., Zhang, Q., Wu, Z. & Nazar, L. F. A new halospinel superionic conductor for high-voltage all solid state lithium batteries. *Energy Environ. Sci.* **13**, 2056–2063 (2020).

95. Zhou, L., Assoud, A., Zhang, Q., Wu, X. & Nazar, L. F. New Family of Argyrodite Thioantimonate Lithium Superionic Conductors. *J. Am. Chem. Soc.* **141**, 19002–19013 (2019).

96. Ham, S.-Y., Yang, H., Nunez-Cuacuas, O., Tan, D. H. S., Chen, Y. T., Deysher, G., Cronk, A., Ridley, P., Doux, J. M., Wu, E. A., Jang, J. & Meng, Y. S. Assessing the critical current density of all-solid-state Li metal symmetric and full cells. *Energy Storage Materials* **55**, 455–462 (2023).

97. Doux, J. M., Nguyen, H., Tan, D. H. S., Banerjee, A., Wang, X., Wu, E. A., Jo, C., Yang, H. & Meng, Y. S. Stack Pressure Considerations for Room-Temperature All-Solid-State Lithium Metal Batteries. *Advanced Energy Materials* **10(1),** 1903253 (2020).

98. LePage, W. S., Chen, Y., Poli, A., Thouless, M. D. & Dasgupta, N. P. Sodium mechanics: effects of temperature, strain rate, and grain rotation and implications for sodium metal batteries. *Extreme Mechanics Letters* **52**, 101644 (2022).

99. Ridley, P., Nguyen, L. H. B., Sebti, E., Han, B., Duong, G., Chen, Y. T., Sayahpour, B., Cronk, A., Deysher, G., Ham, S. Y., Oh, J. A. S., Wu, E. A., Tan, D. H. S., Doux, J. M., Clement, R., Jang, J. & Meng, Y. S. Amorphous and Nanocrystalline Halide Solid Electrolytes with Enhanced Sodium-Ion Conductivity. *Matter* **7(2),** 485-499 (2024).